Enabled primarily controls filopodial morphology, not actin organization, in the TSM1 growth cone in *Drosophila*

Hsiao Yu Fang¹, Rameen Forghani¹, Akanni Clarke¹, Philip G. McQueen¹, Aravind Chandrasekaran^{1,2}, Kate M. O'Neill^{1,3}, Wolfgang Losert³, Garegin A. Papoian², and Edward Giniger¹

Affiliations:

- ¹ National Institute of Neurological Disorders and Stroke, National Institutes of Health, Bethesda, MD, 20892
- ² Department of Chemistry and Biochemistry, University of Maryland, College Park, MD, 20752
- ³ Institute for Physical Sciences, and Department of Physics, University of Maryland, College Park, MD, 20752

Running title:

Live imaging ena function in axons

Summary statement:

We dissect the function of the actin polymerase, Enabled, in axon growth by live-imaging of actin dynamics and axon morphology of the TSM1 neuron in its native environment in vivo.

Keywords:

Axon guidance, Live imaging, Actin dynamics, Drosophila, Abl, filopodia

Abstract

Ena/VASP proteins are processive actin polymerases that are required throughout animal phylogeny for many morphogenetic processes, including axon growth and guidance. Here we use in vivo live imaging of morphology and actin distribution to determine the role of Ena in promoting the growth of the TSM1 axon of the *Drosophila* wing. Altering Ena activity causes stalling and misrouting of TSM1. Our data show that Ena has a substantial impact on filopodial morphology in this growth cone but exerts only modest effects on actin distribution. This is in contrast to the main regulator of Ena, Abl tyrosine kinase, which was shown previously to have profound effects on actin and only mild effects on TSM1 growth cone morphology. We interpret these data as suggesting that the primary role of Ena in this axon may be to link actin to morphogenetic processes of the plasma membrane, rather than for regulating actin organization itself. These data also suggest that a key role of Ena, acting downstream of Abl, may be to maintain consistent organization and reliable evolution of growth cone structure, even as Abl activity varies in response to guidance cues in the environment.

Introduction

As a nervous system develops, each neuron extends an axon to connect with downstream elements of its neural circuit. In this process, the path followed by each growing axon is directed by chemical and physical cues in its extracellular environment {Dickson, 2002 #9;Tessier-Lavigne, 1996 #38}. These cues are detected and processed, in large part, in a sensory and motile structure at the tip of the growing axon, called the growth cone {Lowery, 2009 #27;Dumoulin, 2021 #80;Stoeckli, 2018 #81}. One of the key cytoplasmic signaling mechanisms that integrates signals in the growth cone is the Abl protein tyrosine kinase and its associated signaling network {Bradley, 2009 #3;Lanier, 2000 #24;Moresco, 2003 #28}. Abl is a key element downstream of many of the common, conserved cell surface receptors that direct axon growth and guidance in organisms across the animal kingdom, including DCC, Robo, Eph family receptors, Plexins, integrins, and others {Deinhardt, 2011 #65;Garbe, 2007 #66;Hsouna, 2003 #67;Forsthoefel, 2005 #68;Yu, 2001 #69;Grossman, 2013 #70}. Abl is also an upstream regulator of many aspects of cytoskeletal organization, including polymerization, branching,

bundling, severing, and contractility of actin networks, through processes that are mediated by Ena/VASP proteins, Arp2/3, cofilin, Myosin II, and other actin regulatory factors {Lanier, 2000 #24;Bradley, 2009 #3}. This makes Abl a uniquely informative tool for dissecting the molecular mechanisms by which external signals generate neuronal morphology and connectivity.

One excellent system to connect Abl signaling to cytoskeletal dynamics and growth cone motility in vivo is provided by simultaneous live imaging of fluorescent markers for actin and plasma membrane in the extending TSM1 sensory axon of the developing *Drosophila* wing {Clarke, 2020 #6;Clarke, 2020 #7}. Previous studies have revealed, first, that the TSM1 growth cone is a protrusive, filopodial domain near the leading tip of the axon. The position of this domain is determined by the presence of a local mass of actin in this portion of the axon shaft, which provides the raw materials required to make and maintain the growth cone filopodia. That actin mass undergoes constant, stochastic fluctuations in length, but with a spatial bias that progressively advances the position of the actin mass over time. Forward motion of the actin, however, necessarily also advances the region that is capable of supporting a high density of filopodia, ie., it advances the morphological structure that we recognize as the growth cone. Those experiments further revealed that the role of Abl kinase is to coordinate the stochastically fluctuating expansion and compaction of the actin network, maintaining the actin as a coherent mass and promoting its orderly, net advance down the axon, toward the axon tip. Specifically, increased Abl activity causes net expansion of the actin mass, while decreased Abl causes net compaction. Thus, a pattern of guidance cues that generates a gradient of Abl activity across the length of a growth cone could, in principle, cause preferential expansion of actin at the leading edge of the growth cone and compaction at the trailing edge. This would produce net advance of the actin mass over time, and therefore net advance of the morphological growth cone and growth of the axon.

While experiments to date have characterized the effect of Abl on the spatial distribution of actin in the TSM1 growth cone, it is now essential to dissect the molecular mechanism

downstream of Abl by which the effects of the kinase control the distribution of actin. The best characterized, and most direct, effector linking Abl to actin dynamics is the actin polymerase, Enabled (Ena) {Gertler, 1995 #39; Krause, 2003 #45}. Ena promotes growth of actin filaments, both as a processive polymerase that juxtaposes G-actin monomers to the barbed ends of Factin filaments (Winkelman, 2014 #46), and also by antagonizing the binding of actin filament capping proteins{Bear, 2009 #44;Gates, 2009 #48}. Ena also bundles the tips of actin filaments, in part by forming tetramers that link adjacent filaments (Bruhmann, 2017 #64; Blanchoin, 2014 #79}. Ena has profound effects on cell morphology. Overexpression of Ena stimulates formation of filopodia in many systems, though the mechanism by which it does so is complex and context dependent{Krause, 2002 #20;Lebrand, 2004 #50;Trichet, 2008 #51;Gates, 2007 #11}. For example, the properties of filopodia induced by Ena alone can be rather different to those produced in conjunction with formins, such as Drosophila Diaphanous (Bilancia, 2014 #47; Homem, 2009 #49}. Moreover, in some contexts Ena can promote or stabilize lamellipodia, in part by extending the actin filaments that line the leading edge of such structures (Lacayo, 2007 #53;Rottner, 1999 #52}. The effects of Ena on morphogenesis are not determined solely by its direct effects on actin, however. Ena proteins have a conserved EVH1 domain that binds the peptide motif FPPPP (FP4), which is commonly found in adhesive structures, such as focal adhesions{Bear, 2000 #1}. Ena can therefore link the actin cytoskeleton to the plasma membrane. Ena is present in axons and has demonstrated effects on axon growth and guidance in vitro and in vivo{Lebrand, 2004 #50; Wills, 1999 #42; Kuzina, 2011 #21}. The molecular mechanisms underlying those effects have so far been enigmatic, however{Krause, 2002 #20}. First described in *Drosophila*, Ena has close orthologs in *C. elegans* (UNC-34) {Fleming, 2010 #56; Sheffield, 2007 #55} and in mammals (MENA, VASP (vasodilator-stimulated phosphoprotein) and EVL (Ena- and VASP-like)) that have similar properties{Gertler, 1996 #40}. Ena was first identified as a genetic antagonist of Abl, in that the phenotypes of *Drosophila Abl* mutants can be suppressed by reducing the gene dosage of ena{Gertler, 1995 #39}, and at least some phenotypes of Abl mutant Drosophila seem to be produced by mislocalization and/or hyperactivity of Ena protein{Grevengoed, 2003 #14;Grevengoed, 2001 #15;Kannan, 2014 #62}. Genetic tests show that ena acts downstream of Abl, and consistent with this, Abl regulates Ena

activity, in part, by phosphorylation of conserved tyrosine residues of Ena protein {Comer, 1998 #8}. This cannot be the entire mechanism by which Abl regulates Ena, however, as an Ena derivative lacking these tyrosines still retains significant activity to perform its Abl-dependent functions in *Drosophila* {Comer, 1998 #8}.

Here we perform live imaging of axon morphology and actin distribution in TSM1 axons growing in their native environment of the developing *Drosophila* wing, both in wild type, and upon increase or suppression of Ena activity in the neuron. We find that altering Ena activity has a substantial effect on filopodial number and length, but that the TSM1 growth cone is far more sensitive to reduction of Ena from its wild type level than it is to increase of Ena. The effects of Ena on the distribution of actin are quantitatively much more modest than those on filopodial morphology, though a sensitive analytical method reveals that reducing Ena activity tends to broaden the actin distribution relative to higher levels of Ena. This is consistent with our previously published analysis of the effects of Abl in TSM1, but it is striking that Abl had a far more pronounced effect on actin than on morphology, opposite to our observations here of the consequences of altering Ena. Moreover, as for Abl, we find that either increasing or decreasing Ena activity causes the temporal evolution of the actin distribution to be less orderly and predictable in individual axons than that we observe in wild type. Together, these data suggest that the main role of Ena in the TSM1 growth cone may not be to regulate the actin distribution itself, but rather to modify the linkage of that actin to morphogenetic processes of the plasma membrane. It also suggests that a key function of Ena may be to buffer the downstream consequences of altering Abl activity, thus maintaining the growth cone in an optimal organization for orderly movement while still allowing the cue-directed modulation of Abl activity, and thus actin dynamics {Chandrasekaran, 2022 #71;Chandrasekaran, 2022 #72}, that is necessary to produce guided axon growth.

Results

We performed live imaging of the TSM 1 axon as it grows through the *Drosophila* wing, much as we have described previously {Clarke, 2020 #6;Clarke, 2020 #7} (Fig 1A; Suppl Fig 1). Wing imaginal discs were dissected ~9hrs after the onset of metamorphosis (APF; after puparium formation), mounted in culture media, and imaged for 90 minutes by collecting z-stacks using spinning disc confocal microscopy (interframe interval = 3 min). Membrane and actin distribution, respectively, were visualized by co-expression of CD4-td-Tomato and LifeAct-eGFP, both under control of *neuralized-GAL4* (*neur-GAL4*). Axon morphology was traced in three dimensions and growth cone parameters were quantified as described previously {Clarke, 2020 #6;Clarke, 2020 #7}, including both morphological features, and actin distribution along the axon shaft (measured by radial integration of LifeAct intensity as a function of position along the axon)(Fig 1 B – D; measured parameters are listed in Fig 1C, shown schematically in Fig 1D, and described in detail in Fig 1 legend and in the Methods). Note that, for consistency, all projections from the axon will be referred to below as "filopodia" irrespective of their caliber, lifetime, or potential invasion by microtubules.

Properties and dynamics of the wild type TSM1 growth cone

Live imaging of TSM1 revealed the growth cone to be a domain of three-dimensional filopodial protrusiveness with only very rare indications of lamellipodial structures. As reported previously for TSM1 {Clarke, 2020 #6}, visual inspection of the movies showed no obvious signs of significant substratum adhesion. For example, filopodia were splayed as broadly in the z-axis as they were in x- and y-, both the axon shaft and individual filopodia were commonly observed to shift laterally in position relative to the substratum between time points, and the tips of individual filopodia, including the highly dynamic leading filopodia, showed substantial fluctuation in position between time points, suggesting that they are not strongly anchored to the substratum. In addition, we could not detect any consistent relationship between localization of actin in the growth cone and localization of focal adhesion proteins, such as zyxin (A. Clarke and EG, data not shown). We did find, however, that the protrusive region of the axon, the morphological "growth cone", contained a high local concentration of actin intensity in the axon shaft, such that the position of the window containing the peak density of filopodial

protrusions (here called "the filopodial peak") correlated roughly with the position of the window containing the maximum, integrated amount of total actin intensity (here called "the actin peak"; Fig 2A)(R = 0.7; p < 10^{-4} ; Spearman correlation). When examined in detail, however, we found that the positions of the filopodial peak and the actin peak, while correlated, are not coincident. Rather, the position of the peak of filopodial density tended to lag significantly behind the peak of actin intensity (by $5.2 \pm 0.7 \,\mu m$; mean +/- SEM (median = $1.1 \,\mu m$, p < 0.0001; Wilcoxon signed-rank; Fig 2B)). Moreover, the magnitude of this offset between the positions of the actin and filopodial peaks in any given image correlated with the amount by which each one then advanced in the next frame. Thus, for example, when the actin peak led the filopodial peak by a large amount in one image, we tended to observe greater advance of the filopodial peak in the subsequent image (Fig 2C)but less advance of the actin distribution or even its regression, in that following image (Fig 2D). As discussed elsewhere, this is consistent with data published previously suggesting that progressive advance of the protrusive filopodial domain over time occurs as a response to the change in the local availability of actin as the actin mass moves forward down the axon {Clarke, 2020 #6;Goncalves-Pimentel, 2011 #74}.

Detailed examination of actin distribution in the TSM1 growth cone revealed that the mass of actin undergoes constant, seemingly stochastic, fluctuations in position, but with a small, yet persistent, forward bias that produced net advance of the actin distribution over time (Fig 2E). Thus, while the position of peak actin intensity took a significant number of steps both forward and backward in any given trajectory, and these could be of roughly comparable magnitude, the net effect over the course of imaging was that the peak position of actin intensity preferentially moved forward along its trajectory. These fluctuations in peak position were also associated with fluctuations in the spatial extent of the actin peak along the axon (the "length" of the actin peak; Fig 2F (compare Fig 1D)), suggestive of the actin "inchworming" forward over time as it moved forward in the axon shaft. In essence, a combination of preferential forward expansion of the leading edge of the actin mass, together with preferential compaction from the rear, causes the length of the actin mass to fluctuate around a mean, but with net forward motion of the mass as a whole. Together with other experiments {Clarke, 2020 #6}, these

observations demonstrate that TSM1 growth cone advance is correlated with forward-biased fluctuations of the actin distribution. This interpretation is also consistent with the observation that the magnitude of the offset between the peaks of actin vs filopodial density in any given image correlated with the length of the actin peak (Fig 2G; see also {Clarke, 2020 #6;Clarke, 2020 #7} for further discussion of this hypothesis).

Overall morphological phenotypes from enabled gain- and loss-of function

We next determined the effect produced on TSM1 morphology and motility when we altered the activity of Enabled (Ena) in the neuron by taking advantage of the yeast transcriptional activator, GAL4, expressed under control of regulatory sequences of the gene *neuralized* (*neur-GAL4*). Ena activity was either increased, by expressing a *UAS_G-ena(WT)* transgene, or suppressed, by sequestering Enabled protein to mitochondria using expression of a *UAS_G-FP4-mito* transgene. FP4-mito has an Ena binding motif, including the sequence FPPPP, linked to a mitochondrial targeting sequence. It has been validated extensively in multiple organisms and developmental contexts, and shown to provide an effective (albeit not perfect) mimic of the *ena* genetic loss-of-function condition {Bear, 2000 #1;Gates, 2007 #11;Kuzina, 2011 #21;Lebrand, 2004 #50}. Its use here allows us to inactivate Ena selectively in neural tissue and bypass the lethality of a genetic null mutant of *ena*.

We first verified the efficacy of our genetic reagents to manipulate ena activity in TSM1. To validate the effectiveness of the UAS-ena transgene for producing a gain-of-function phenotype when expressed with neur-GAL4, we needed a well characterized ena overexpression phenotype that could be assayed in neurons $in\ vivo$. In Drosophila photoreceptors, Ena protein is associated with the cis-Golgi and overexpression of Ena leads to clustering of the protein, and of the Golgi, and their relocalization to the basal part of the cell body {Kannan, 2014 #62}. Consistent with this, expression of UAS_G -ena(WT) under control of neur-GAL4 produced a similar pattern of clustering and relocalization of Ena in photoreceptors, demonstrating that expression of the transgene is effective for enhancing Ena activity (Fig 3B, compare control in Fig 3A; see also Suppl Fig 2A, B). Similarly, we wished to verify the effectiveness of the FP4-

mito-eGFP transgene for producing an ena loss-of-function phenotype. Reducing ena activity has relatively mild effects on overall axon patterning in the Drosophila embryo (Gates, 2007 #11}, but it produces a specific and well-characterized misrouting of motor axons of the "b" branch of the intersegmental nerve (ISNb) in the embryo whereby these axons fail to form a separate fascicle and instead remain part of the main ISN (called a "bypass" phenotype (Wills, 1999 #42}). We therefore examined ISNb targeting in embryonic neurons expressing UAS_G-FP4mito under the control of neur-GAL4 and observed ISNb axons following the aberrant "bypass" trajectory that is typical of ena mutants, validating the activity of this reagent in Drosophila neurons (Fig 3D, compare control in Fig 3C). To verify that these transgenes are expressed effectively specifically in TSM1 when placed under control of neur-GAL, we performed anti-Ena antibody staining of early prepupal wing discs expressing UAS_G-ena(WT) or UAS_G-FP4-mito-eGFP under the control of neur-GAL4. As expected, in wings expressing UAS-ena under control of neur-GAL4 we observed enhanced Ena protein immunoreactivity in wing margin sense organs in general, and TSM1 in particular (Fig 3F, compare control in Fig 3E). In contrast, upon expression of UAS-FP4-mito-eGFP with neur-GAL4, the endogenous Ena protein (visualized by anti-Ena immunoreactivity) became concentrated in small, dense puncta that colocalize with mitochondria in TSM1, as identified by the localization of the FP4-mito-eGFP protein itself. Such puncta of Ena immunoreactivity were not observed in control wings (Fig 3I, compare control in Fig 3H). Finally, the eponymous mutant phenotype of enabled is its suppression of mutant phenotypes observed in Abl loss-of-function. We therefore compared the frequency of defects in the mature trajectory of TSM1 in wings of flies expressing RNAi against Abl (under control of neur-GAL4) to that in Abl RNAi flies that co-express UAS_G-FP4-mito. Expression of Abl RNAi in TSM1 causes a variety of axonal defects, primarily axon stalling {Clarke, 2020 #6}. We found that suppression of Ena activity with FP4-mito reduced the frequency of Abl RNAiinduced TSM1 defects by nearly 50% (19% vs 37%; p = 0.009; chi-squared; Fig 3M). Typical examples of the TSM1 axonal phenotype under these conditions are shown in Fig 3 J-L, and the phenotype is quantified in Fig 3M. These data verify that expressing FP4-mito suppresses the Abl loss-of-function axonal phenotype in TSM1.

It was also of interest to investigate the localization of Ena protein in the TSM1 growth cone. Unfortunately, anti-Ena immunostaining of fixed, wild type wing discs was not informative on this point since the Ena immunoreactivity of the axon and growth cone was obscured by the high levels of Ena immunoreactivity in the closely-associated epithelia of the wing (Suppl Fig 2C). However, we were able to detect reliably the enhanced Ena immunoreactivity in TSM1 growth cones expressing UAS-ena (Fig 3G). Here we saw Ena signal throughout the growth cone above the level in the associated epithelia, both in the core of the growth cone and in filopodia. In contrast to what has been reported in other contexts, however, {Lebrand, 2004 #50; Gates, 2007 #11} we usually did not observe evidence for accumulation of Ena at the tips of filopodia. Ena signal did not seem to be excluded from the distal parts of filopodia, but neither did we generally observe it concentrated there (Fig 3G). This may perhaps be related to the failure to see adhesive interactions of filopodial tips with the substratum (see above). We emphasize, however, that this analysis of Ena localization reports the distribution of the protein when it is overexpressed. We cannot comment on Ena subcellar distribution in wild type TSM1 growth cones. Ena protein was also not discernable above the epithelial background in TSM1 growth cones when expressing FP4-mito (Suppl. Fig 2D).

Visualizing the terminal phenotype of wings expressing Ena-modifying transgenes revealed that altering Ena activity disrupted the overall patterning of the TSM1 axon at only modest expressivity, just as has been observed for many embryonic axons {Gates, 2007 #11}. Expression of *UAS-ena* with *neur-GAL4* caused terminal defects in 19% of wings examined while expression of *UAS-FP4-mito-eGFP* caused defects in 28% (Fig 3 N-P; quantified in Fig 3Q; $n \ge 55$ wings for each genotype). Most of these defects were failures of the axon to reach its target zone on the L3 nerve (termed "stalls"), often with neurites projecting from the tip of the stalled axon. In a small number of cases other kinds of defects were observed, such as the axon projecting along an aberrant path, leading to fasciculation with L3 at a position distant from its normal target zone. The average rate of axon growth was not significantly different in the three genetic backgrounds (average growth rate = $0.21 \pm 0.15 \,\mu\text{m/min}$ in wild type vs $0.13 \pm 0.35 \,\mu\text{m/min}$ in *UAS-FP4-mito* and $0.18 \pm 0.11 \,\mu\text{m/min}$ in *UAS-ena*; differences not significant:

p=0.42; this and all parameter values are presented in the text as mean ± SEM; see Statistical Methods for details of how statistical significance was calculated)(Fig 4A). Examining the pattern of motility in greater detail revealed that the mode of growth cone movement in the altered-Ena conditions resembled that of wild type, displaying a stuttering, inconsistent pattern of advance, overlaid by stochastic fluctuation of the length of the actin mass in the growth cone, and with the actin peak tending to lead the peak of projection density (Fig 4 B, E-H; typical examples of growth cone morphology for *neur-GAL4*; *UAS-FP4-mito-eGFP* and *neuro-GAL4*; *UAS-ena* are shown in Fig 4 C and D, respectively).

Effects of Ena on actin distribution and filopodial pattern in TSM1

We next examined the effects of Ena on the detailed pattern of actin distribution and filopodial morphology in TSM1. Whereas we had found previously {Clarke, 2020 #6} that altering Abl kinase activity primarily modulates the distribution of actin, with only modest effects on growth cone morphology, we now found that the effects of manipulating Ena were opposite, primarily modifying morphology, with only modest effects on actin distribution (Fig 5). First, we found that the amount of active Ena correlated directly with the number and total length of filopodia but not with their average length or branching complexity, as we now describe. Neurons overexpressing Ena (UAS-ena) had 35.6+2.1 filopodia, vs 16.9+0.7 filopodia for UAS-FP4-mito (mean \pm SEM; p < 10^{-4} ; ANOVA) (Fig 5A). Similarly, increasing Ena also enhanced the total length of filopodial projections per axon (254.5+18.1 μm for UAS-ena vs 145.9+7.6 μm in UAS-FP4mito; p < 10^{-4} ; ANOVA) (Fig 5B). For each of these parameters, comparison to wild type reveals that the neuron was far more sensitive to reduction of Ena activity than to its increase, with reduction accounting for 85% of the difference in mean filopodial number between Ena overexpression vs FP4-mito mediated suppression, and essentially 100% of the difference in total filopodial length, (filopodial number in wild type = 30.7±2.9; total filopodial length = 256.2±26.9). Perhaps surprisingly, average filopodial length was not reduced upon expression of UAS-FP4-mito, as the decrease in total filopodial length was in proportion to the decrease in filopodial number (average filopodial length 8.9+0.4 μm in UAS-FP4-mito vs 8.2+0.1 in wild type; difference not significant: p=0.3; ANOVA) (Fig 5C). In contrast, the combination of

increased filopodial number without a corresponding increase in total filopodial length in the Ena-overexpressing condition manifested as a significant <u>decrease</u> in average filopodial length $(7.2+0.1 \, \mu m; \, p < 10^{-4} \, \text{compared to wild type}; \, \text{ANOVA})$. This observation is different from findings in other systems, a point we will come back to in the Discussion. Finally, in contrast to filopodial number and length, altering Ena activity did not change the complexity of filopodial branching, as the average projection order (primary, secondary, tertiary, etc.) was not altered by changes in *ena* activity $(1.44, 1.42, \, \text{and} \, 1.46, \, \text{respectively}, \, \text{for wild type}, \, \text{UAS-FP4-mito} \, \text{and} \, \text{UAS-ena}; \, p=0.62 \, \text{across genotypes}; \, \text{ANOVA}) (\text{Fig 5D}).$

We next quantified the effect of Ena on parameters of actin organization. One of the key actin features of the growth cone shown previously to be regulated by Abl is the length of the actin peak {Clarke, 2020 #6}. Here, for Ena, we saw a trend toward a small shift in the expected direction, with suppression of Ena activity perhaps causing expansion of the actin peak relative to Ena overexpression (14.1μm in UAS-FP4-mito vs 11.9μm in UAS-Ena; 95% confidence intervals 11.8-16.5 vs 10.7-13.2, respectively; Fig 5E). This is consistent with the expansion of the actin peak seen upon overexpression of Abl, the Ena antagonist. As we found for the filopodial parameters, the majority of the difference between the two altered Ena conditions derived from the effect of Ena suppression (WT = $12.2\mu m$; 95% CI 8.8-16.0). Quantitatively, however, the apparent effect of Ena on the length of the actin peak was rather small in magnitude and did not achieve formal statistical significance. Therefore, to test this apparent trend, we performed a more sensitive analysis of the spatial distribution of actin along the axon, using wavelet analysis. The wavelet transform quantifies how LifeAct fluorescence intensity is distributed along the axon, for example, is it distributed homogeneously or is it clumped, and what is the spacing between concentrations of actin along the length of the axon? Thus, the presence of small, dense clumps of actin would give rise to increased values for the coefficients of high-order wavelets, while spreading of actin across large, multi-micron spatial scales would be reflected in enhanced values of lower-order wavelets (For a more detailed explanation of wavelets see Suppl methods and also {Clarke, 2020 #7}). It is important to note that the amplitude values of the wavelet transform derive from the entire actin

distribution, across the whole length of the axon, for any given time point. It is not calculated from selected, individual features of a distribution. In addition, wavelets are calculated separately for each of the time points for a given cell and these can then be averaged together to yield a picture of the properties of that axon across the entire imaging session. Similarly, wavelet amplitudes can be averaged together from multiple cells to give a quantitative picture of the properties of a given genotype. Here we find that plotting the ratio of (wavelet amplitude)² for (*UAS-FP4-mito/UAS-ena*) vs wavelet order reveals that reducing Ena activity leads to a significant enhancement of the contribution of a narrow range of wavelets, peaking at 5th order (p<10⁻⁴; ANOVA), corresponding to separation of actin density at a spatial scale corresponding to \sim 6.5 – 25.6 μ m (Fig 5F; Suppl Fig 3). Stated otherwise, the wavelet analysis shows that reducing Ena activity causes actin to spread out at this multi-micron scale of separation, consistent with the increased length of the actin peak observed by direct measurement as Ena activity is decreased, and also consistent with our earlier wavelet analysis of the Abl gain-of-function condition {Clarke, 2020 #7}.

The other major feature of actin shown previously to be regulated by Abl in TSM1 is its degree of consistency, that is, the extent to which the distribution of actin observed at one time point predicts what the distribution will be at a subsequent time point. We quantify this feature with a property termed the Jensen-Shannon divergence. To calculate the divergence of the actin distribution between two time points, one compares the magnitude of the actin signal at each position along the axon at one time with the magnitude at the corresponding position at another time. If two distributions are identical, the divergence will be 0. If two distributions have no overlap, the divergence will be 1. This metric therefore gives a quantitative measure of how much the distribution of actin has changed between any two selected times for a given cell. Note that this is simply an unbiased comparison of the spatial distribution of actin intensity measured along the length of the axon. It does not incorporate any derived quantities or assumptions about growth cone features. For each of the wild type trajectories we analyzed, we found that the divergence between the actin distribution at the start of imaging (t=0) vs the distribution at the next time point (t=1) is relatively small, but that the divergence increases

systematically as the starting actin distribution is compared to later and later time points of the same trajectory (Fig 5G). In contrast, if we alter Ena activity, either by suppression with FP4-mito or by overexpression of Ena, that predictability is degraded significantly (Fig 5 H-J; Suppl Fig 4). There are still some trajectories in the altered Ena conditions that show consistent increase in divergence with time, but there are also trajectories where divergence is uniformly high, or changes with time in unpredictable ways. Thus, we see that the dynamic reliability of the evolution of the actin pattern is disrupted when we perturb the activity of Ena.

Analysis of the global effects of Ena on the TSM1 growth cone by PCA

We know from our previous analysis of Abl that single growth cone parameters with small individual responses to perturbation can nonetheless contribute to robust consequences because of consistent correlations among some growth cone features. We therefore expanded our analysis of Ena by querying the pairwise correlations of growth cone parameters, as well as examining the global effects of the whole set of growth cone features in an unbiased principal components analysis (PCA).

Correlations between individual pairs of growth cone parameters that were found to be significant across all three genetic conditions identified core features of a well-formed growth cone and of effective growth cone advance (Fig 6A; Suppl Fig 5). Thus, for example, filopodial number, total filopodial length, and the filopodial branching complexity (average projection order), showed significant three-way correlation in all three genotypes, suggesting that this nexus reflects a consistent feature of growth cone cell biology (Fig 6B). Consistent correlation of these three features was also observed in our previous study of TSM1 {Clarke, 2020 #6}. Moreover, as discussed above for wild type, the offset between the actin and filopodial peaks also showed significant correlation with the length of the actin mass in both altered-Ena genotypes, as well as negative correlation between the magnitude of that offset in a given time point and the degree of advance of the actin in the following interval, both suggesting a stepwise, inchworming mode of axon growth. Also consistent with this, both altered-Ena conditions recapitulate the positive correlation of the offset between the positions of the

filopodial and actin peaks in any given image vs advance of the filopodial distribution in the time step that followed (Fig 6 C, D), which was shown above to be a consistent feature of wild type TSM1 axon growth (Fig 2C).

Unbiased global analysis of the interactions among growth cone parameters by PCA yielded additional insight into axon structure and dynamics, and how they are modulated by Ena (Fig 7A-F). Our previous study of TSM1 revealed that wild type growth cones could be classified into two related, but distinct, morphological classes, one with a simpler filopodial branching structure and the other more complex {Clarke, 2020 #6}. The current wild type dataset reproduces that effect. Thus, in the current wild type dataset, morphological features of filopodia dominate PC1: filopodial number, total filopodial length and filopodial branching complexity. Examination of the PCA reveals that the WT cells fall into a bimodal distribution of PC1 values with the time points from three of the wild type trajectories having PC1 values nearly exclusively less than -0.5 and the time points from the other seven trajectories almost entirely above that value (Fig 7G, H), reproducing the categorical distinction into two classes that was observed previously. Suppression of Ena activity by expression of FP4-mito shifted the distribution completely to the simpler morph (higher values of PC1; Fig 7D, I; Suppl Fig 6A). In contrast, however, upon overexpression of Ena, while the mean value of PC1 did not change by a statistically significant amount, the distribution essentially collapsed to a single peak, erasing any evidence for a categorical distinction between two different morphological classes (Fig 7 E, J; Suppl Fig 6A). The total range of possible PC1 values was nearly as broad as in wild type, but the most common morphology in *UAS-ena* was essentially intermediate between the two forms observed in the wild type data. We also examined PC2, which was dominated by the length of the actin distribution, and to a lesser degree by the closely correlated length of the filopodial distribution. The three genotypes showed no significant difference in the means of the distributions of PC2 values (Suppl Fig 6B), reinforcing the interpretation that Ena has limited effects on the actin distribution itself, in contrast to its strong effects on morphological features of TSM1.

Discussion

Here we have used live imaging of the TSM1 axon in the developing *Drosophila* wing to investigate the role of the processive actin polymerase, Ena, in the molecular mechanism of axon growth and guidance, and to compare it with our previous analysis of the effects of the Ena regulator, Abl tyrosine kinase {Clarke, 2020 #6;Clarke, 2020 #7}. We find that Ena has a significant effect on the number of filopodial projections in the wild type growth cone, but much less effect on their length, or on where they form. We also observe an asymmetry in the effects of Ena, with suppression of Ena activity producing a large effect on growth cone morphology but increase of Ena having little effect. This may suggest that the wild type level of Ena in this growth cone is already close to saturating for its morphological functions. In contrast to its substantial effects on growth cone morphology, we find that the effect of Ena on the distribution of actin in this growth cone is quite modest. The actin mass at the heart of the growth cone undergoes slight expansion with decrease of Ena activity, but the effect size is not large. Alteration of Ena level also impairs the orderly evolution of the growth cone actin distribution over time. The limited sensitivity of the growth cone actin distribution to the level of Ena, as opposed to the strong effect of Ena on morphological features, is in striking contrast to the effect of Abl, which has a profound impact on the distribution of actin but only modest effects on overall growth cone morphology. These observations suggest that Ena may be more important for the linkage of actin to the membrane and downstream morphogenetic processes of this axon than it is for the distribution of the actin itself. Taken together, our data also suggest that the balance of Ena with other factors regulated by Abl may serve to buffer the effects of Abl on filopodial patterning, thus maintaining an optimal growth cone organization for orderly axon growth while still allowing Abl to act as a rheostat to vary actin dynamics.

Live imaging of morphology and actin organization in a developing pioneer axon of the *Drosophila* wing, TSM1, recently led us to propose a novel and unexpected model for axon growth and guidance *in vivo* {Clarke, 2020 #6;Clarke, 2020 #7}. We found that the distal part of the axon shaft contains a region with a high local concentration of actin. This actin mass

undergoes constant, stochastic, fluctuations in size, but with a small forward bias that produces net advance of the actin mass over time. Since actin and associated factors are essential for building and maintaining filopodia, advance of the actin mass leads, in turn, to advance of an emergent domain of high filopodial density that is the morphological feature we recognize as "the growth cone". We also showed that Abl tyrosine kinase is a key regulator of actin distribution and dynamics in the growth cone, and thus, indirectly, of growth cone morphology and motility. In the current work, to investigate how Abl produces these changes in actin organization, we have quantified the effects of a core Abl effector, the processive actin polymerase, Ena.

The effects of Ena on growth cone morphology and actin organization in TSM1

Consistent with data from other systems{Krause, 2003 #45}, we found that Ena has a significant impact on the morphology of the TSM1 growth cone in vivo. Varying Ena had a significant effect on filopodial number, with fewer filopodia present under conditions of low Ena activity than with high Ena. Surprisingly, however, nearly all of that effect (85%) was due to the consequences observed upon suppressing Ena; the effect of increasing Ena (relative to wild type) was far more muted. Similarly, varying Ena activity revealed a shift to less total filopodial length with lower levels of active Ena, again with the overall effect dominated by the consequences of Ena suppression. The limited effect of Ena overexpression was unexpected, and may suggest that Ena is present in the wild type TSM1 at a level that is already nearly saturating for Ena function. A significant effect of Ena overexpression was observed, however, upon measuring average filopodial length: the combination of increased filopodial number in UAS-Ena, relative to wild type, without a corresponding increase in total filopodial length, manifested as a significant decrease in average filopodial length (though, curiously, suppression of Ena in this axon did not cause a decrease in average filopodial length, unlike many other systems where Ena has been investigated (Gates, 2007 #11;Lebrand, 2004 #50;Vasioukhin, 2000 #57}). It is not clear why increasing Ena failed to produce a simple dose-dependent increase in average filopodial length in TSM1. It may be that Ena interacts in some complex way with other actin polymerases, such as formins, in the filopodia of this axon {Bilancia, 2014

#47; Homem, 2009 #49}, or that formin levels are regulated in a way that compensates for changes in Ena activity. Alternatively, since we typically did not observe strong accumulation of Ena protein at TSM1 filopodial tips, it may be that Ena functions differently in these nonadherent filopodia in vivo than it does in the highly adhesive contexts where most analyses of Ena/VASP filopodial function have been performed previously {Bear, 2000 #1;Gates, 2007 #11; Grevengoed, 2003 #14; Krause, 2002 #20; Lacayo, 2007 #53; Lebrand, 2004 #50; Rottner, 1999 #52; Vasioukhin, 2000 #57}. In this context, it is interesting to note that in vivo analysis of the C. elegans ena ortholog, UNC-34, in growth cones of VD motoneurons revealed results very similar to those we observe here, in that mutation of UNC-34 reduced filopodial number but had no effect on filopodial length {Norris, 2009 #73}. Despite these Ena-dependent changes in growth cone morphology, however, altering Ena activity produced overt defects in the terminal phenotype of TSM1 in only a modest fraction of wings. This is reminiscent of results from analysis of axon patterning in *Drosophila* embryonic development, where ena gain or loss of function also produce axonal mutant phenotypes only in a limited set of developmental contexts {Wills, 1999 #42; Gates, 2007 #11}, and also of development of retinal axons in Xenopus where Ena is important for arborization of axons, but not for their targeting {Dwivedy, 2007 #58}.

In contrast to these strong effects of Ena on filopodial organization, it was surprising to find that Ena has only rather subtle effects on actin distribution in TSM1. Decreasing the level of available Ena is associated with an increasing overall length of the actin mass in the growth cone, as well as spreading of the actin within that mass, as assayed by wavelet analysis, consistent with the expected complementarity of Ena to the effect of altering Abl. In the case of Ena, however, the effects on actin are quantitatively rather small. This is different from the findings in our earlier analysis of Abl, whose major effect on TSM1 is in regulation of actin organization, with effects of Abl on morphology being much more limited. Consistent with the modest effects of Ena on actin distribution in the current study, altering Ena activity did not significantly alter the average rate of advance of the growth cone actin mass. Moreover, the overall pattern of growth cone dynamics remained the same regardless of the level of Ena

activity, with longitudinal expansion of the actin mass being associated with the instantaneous advance of the actin peak, and the resulting offset between actin mass and filopodial density correlating with subsequent advance of the filopodial peak.

Comparison of TSM1 observations to other experimental and theoretical analyses of Ena

The combination of effects we observe for Ena in TSM1 in some ways match those seen in published analyses of Ena in other systems, but in other ways they were rather unexpected. In contrast to our data here for TSM1, in other systems, Ena has been shown to have substantial effects on actin organization, and Ena overexpression has been shown to induce robust extension of cellular projections. We note, however, that those studies have in general investigated Ena action in cellular contexts dominated by substratum adhesion: epithelia (Gates, 2007 #11; Vasioukhin, 2000 #57}, adherent cells {Bear, 2000 #1; Lacayo, 2007 #53}, and axons growing in an adherent fashion on rigid supports {Lebrand, 2004 #50;Gupton, 2010 #59}. In all of these cases, it may be that interaction of Ena with adhesive structures plays a critical role, feeding back on actin organization in response to morphological inputs. In TSM1, in contrast, our observations do not provide obvious suggestion of a significant adhesive contribution, similar to the limited role of adhesion in studies from other labs investigating motion in compliant, three-dimensional media, both for growth cones and for motile cells{Lammermann, 2008 #23; Santos, 2020 #34}. Indeed, the notion suggested above that a key role of Ena in TSM1 may lie in the linkage of actin to the plasma membrane, rather than in direct effects on actin structure, would agree well with an observation that the protein has generally stronger effects in adhesion-limited cellular contexts{Sheffield, 2007 #55;Vasioukhin, 2000 #57} than it does in TSM1.

The experimental observations made here showing that Ena has relatively modest effects on actin organization agree well with our recent results from computational simulations of actin networks {Chandrasekaran, 2022 #71; Chandrasekaran, 2022 #72}. There, we found that the effects on actin from changing Ena activity were manifested most strongly on fine details of network organization at very short range (sub-micron) length scales, beyond the resolution of

our microscopy of TSM1. In the simulations, modulation of more robust actin nucleators, such as Arp2/3, and contractile elements, such as Myosin II, were required to produce large, mesoscale (multi-micron-level) effects on actin distribution like those that we observe here in the living wing disc, and that we have shown to underlie the mechanism of axon growth and guidance. This suggests that aspects of signaling downstream of Abl that are distinct from its regulation of Ena are likely to play the key role in regulating large-scale actin organization in the growth cone. A strong candidate is Abl-dependent activation of the Rac GEF, Trio, with consequent stimulation of a Rac-WAVE pathway, which we have shown to occur in parallel to the Abl-Ena interaction (Kannan, 2017 #17; Kannan, 2017 #18), and which would be predicted to stimulate the branching actin nucleator, Arp2/3. Moreover, it has been shown that Abl regulates the activity of Myosin II {Dudek, 2010 #60}, another key regulator of the mesoscopic organization of non-polarized actin assemblies in our simulations (Chandrasekaran, 2022 #71). Our computational analysis also suggested a simple mechanistic explanation for how nanometer-scale changes to actin filament length produce multi-micron scale changes in the overall distribution of actin density by modifying the connectivity (percolation) of the actomyosin network {Chandrasekaran, 2022 #72;Chandrasekaran, 2022 #71}.

How and why does altering Ena activity produce terminal mutant phenotypes in TSM1?

While the overt effects of Ena on TSM1 growth cone properties are relatively subtle, they are evidently significant physiologically since we observe defects in the final trajectory of the axon in 20-30% of wings (depending on the manipulation). One good candidate for a cause of those terminal defects is our observation that experimental manipulations increasing or decreasing Ena activity disrupt the reliable evolution of the actin pattern in the growth cone over time. In the wild type axon, the actin peak advances in an orderly way, where the distribution of actin at any given time allows one to predict the global features the distribution will have at subsequent times. In the altered Ena conditions this predictability is lost, stochastically, in a fraction of cells. We speculate that the axons that eventually stall or misroute may be the ones where the orderly progression of actin states fails to occur. The same kind of dynamic instability of the actin pattern was observed in our previous study upon increase or decrease of Abl activity, and

in that case it was also correlated with more generalized disorganization of the actin distribution {Clarke, 2020 #6;Clarke, 2020 #7}. These data are therefore consistent with the hypothesis that modulation of Ena activity may be important to the mechanism by which Abl ensures that transformations of the actin distribution occur in an orderly fashion in the advancing growth cone, and that this consistency is important for reliable axon growth.

There is a second possible reason why wild type Ena activity may be essential for consistent growth of the TSM1 axon. The data reported here show that altering Ena activity, particularly reducing Ena activity, produces strong effects on filopodial pattern in TSM1, in contrast to Abl, which has at most a mild effect on TSM1 filopodial morphology. This is curious, however. If Abl regulates Ena, and Ena strongly modifies morphology, why doesn't altering Abl have a stronger effect on TSM1 filopodial morphology? Our earlier studies of Abl signaling may hint at an explanation. We have shown previously that there are at least two opposing signals downstream of Abl, suppression of Ena, but also activation of a Trio-Rac-WAVE-Arp2/3 pathway, and we have speculated that this pattern of antagonistic regulation of its two key effectors may be critical to Abl function (Kannan, 2017 #17; Kannan, 2017 #18). Activation of Ena promotes filopodial development, as discussed above, but so does activation of Arp2/3 {Goncalves-Pimentel, 2011 #74;Norris, 2009 #73}. It is thought that Arp2/3 promotes formation of sub-membranous, branched actin networks that nucleate the parallel actin filaments that extrude filopodia{Biyasheva, 2004 #2;Korobova, 2008 #61}, and indeed, experimental manipulation of Arp2/3 activity has verified that activation of this protein complex enhances filopodial number in Drosophila growth cones (Sanchez-Soriano, 2010 #33). Therefore, it seems plausible that the antagonistic regulation of Ena vs Arp2/3 by Abl may have the net effect of keeping the local propensity for filopodial extension in the growth cone roughly constant, even as Abl activity changes. Stated otherwise, by this model, a key function behind the complementary regulation of Ena vs Rac-WAVE-Arp2/3 may be to buffer the effects of Abl on filopodial morphogenesis, maintaining the growth cone in an optimal morphological state for continued growth, while leaving Abl activity free to be an adjustable rheostat that can be altered to modulate actin organization in response to external cues, tuned to produce the

directed expansion and compaction of the mesoscale actin network that is the engine for axon growth and guidance.

Experimental Methods

Drosophila stocks

Drosophila stocks *neur-GAL4[A101]* (BDSC 6393), *UAS-LifeAct-eGFP* (BDSC 35544) and *UAS-CD4-td-Tomato* (BDSC 35837) were obtained from the Bloomington Drosophila Stock Center. *UAS-ena* (untagged) and *UAS-FP4-mito-GFP* were obtained from Julie Gates (Bucknell University) and Mark Peifer (UNC-Chapel Hill). Note that under our conditions of imaging (low intensity of the 488nm laser to limit photodamage and low GFP detector gain to prevent saturation of axonal LifeAct-eGFP signal; see below), GFP fluorescence was not detectable in the axon upon expression of *FP4-mito-eGFP*. Flies were raised on standard cornmeal/molasses food (KD Medical, Columbia MD).

Microscopy and antibody staining

Fixed samples were used only to generate the anatomical reference images of Fig 1A and controls for reagent activity in Fig 3. To prepare the early-prepupal image, white prepupae (WPP) were collected, aged 8 hours at 25°, then dissected and fixed for 25′ in PBS containing 4% formaldehyde and 0.1% glutaraldehyde. Wings were then washed in PBS, transferred to PBS + 0.3% Triton X-100 (EM Sciences, Hatfield, PA), blocked, incubated for 90′ with TRITC-anti-HRP (Jackson ImmunoResearch, West Grove, PA; cat# 323-025-021; dilution 1:100), washed, and mounted in Prolong Gold. To visualize Ena protein in prepupal wing discs, essentially the same fixation and staining protocol was used, except that glutaraldehyde was omitted from the fix and the primary antibody was anti-Enabled antibody (mAb 5G2, 1:50 dilution, Developmental Studies Hybridoma Bank, Iowa City, IA), followed by donkey-anti-mouse secondary (AlexaFluor, 1:500 dilution, Jackson ImmunoResearch)) To prepare the late-stage (pupal) image and samples for scoring the terminal phenotype of TSM1, WPP expressing *CD4-td-Tomato* under control of *neur-GAL4* were collected and aged 20hr at 25°. Pupae were removed from the pupal case and fixed in PBS containing 4% formaldehyde for 25′, RT. After washing, fixed pupae were dehydrated in 100% ethanol and stored in ethanol for at least 24 hrs at 4°. Pupae were then

rehydrated in PBS + 0.3% Triton, wing discs were dissected and mounted in Vectashield (ThermoFisher). Widefield microscopy was performed with an AxioImager Z1 microscope, and image stacks were deconvoluted and processed in Zen.

Live imaging

Live imaging was performed by a modification of the method described in Clarke, et al {Clarke, 2020 #6}. WPP of the appropriate genotype were collected and aged 8hrs at 25°. Wing discs were dissected in fresh culture media (Schneider's *Drosophila* media (Life Technologies) containing 10% fetal bovine serum (Gibco)). Wing discs were transferred to a drop of culture medium (~15µl) in the middle of an 18 x 18mm #1.5 coverslip and mounted by the method of Rusan and coworkers ({Lerit, 2014 #41}; see also Suppl Fig 1). In brief, discs were transferred in a minimum volume of culture medium using a pipet tip that had been treated with Sigmacote (Sigma-Aldrich, St. Louis, MO) and pre-blocked by triturating contents of the pupal abdomen. Small (~10-15µl) drops of #700 halocarbon oil (Sigma) were placed at the corners of the coverslip and it was stuck to the underside of a gas-permeable Lumox 35 culture dish (Sarstedt), which was then inverted. Media and oil were allowed to spread, and a kimwipe was used to wick away media and oil until wings were physically restrained but not crushed. Additional oil was used as needed to seal the edges of the coverslip. Up to 5 discs were mounted per imaging chamber. Imaging was performed on an inverted microscope, with imaging chamber right-side up and filled with ~3 ml culture media (to avoid reflection at the surface of the dish).

Imaging was performed with a Zeiss AxioObserver Z1 spinning disc confocal microscope with a 25° temperature-controlled stage. Z-stacks were taken at $0.8~\mu m$ spacing with a 63x/1.2~NA water immersion lens. Typically, two discs were imaged at once, using the multipoint feature of the software. Imaging runs were 90 minutes with 3' between initiation of successive frames. Images were not deconvoluted as previous experiments showed that deconvolution corrupts the information content of the images {Clarke, 2020 #6}.

n = 10 control trajectories (*neur-GAL4*), 10 trajectories of *neur-GAL4*; *UAS-FP4-mito-eGFP*, and 13 trajectories of *neur-gAL4*; *UAS-ena*. 31 time steps were collected for each trajectory with a 3' interval between the initiation of successive z-stacks.

Segmentation of images and quantification of growth cone parameters

Tracing of axons and quantification of LifeAct intensity were performed precisely as described in Clarke, et al {Clarke, 2020 #6}. In brief, three-dimensional tracing in Imaris (Bitplane, version 8 or 9) was first performed of just the axon shaft and converted to Nikon ICS format. This was imported into MIPAV, which generated an SWC format description of the axon (plug-in: *Drosophila creates SWC*), and then calculated the LifeAct intensity as a function of position along the axon by summing signal intensity in sequential frustums centered on the axon shaft (plug-in: *3D SWC stats*). Complete tracing of all projections was then performed in Imaris, and again converted to ICS format and imported to MIPAV for preparation of an SWC file. During tracing, care was taken to begin the trace at a specific position of the proximal axon that could be identified consistently in all frames of the trajectory.

Parameters describing features of morphology and actin distribution were calculated as described previously {Clarke, 2020 #6}. Custom Python scripts were written to calculate the desired parameters for each image from the SWC file of projections and from the spreadsheet of actin intensity as a function of position in the axon shaft. Parameters are listed in Fig 1C. These include the total number of filopodial projections from the axon shaft, total length and average length of filopodia, and average order of filopodial projections. To calculate filopodial density along the axon, higher order projections were assigned to the position of their parent primary projection. The position of maximum filopodial density, and of maximum actin intensity, were identified separately using 5µm sliding windows (advanced in 1µm steps). It was shown previously that results are robust to the choice of window length (1-10µm; {Clarke, 2020 #6}). As previously, the "length" of the protrusive filopodial zone of the axon was calculated as the square root of the second moment of the distribution of filopodial density about the position of the window with the maximum value, and the "length" of the region of elevated

actin concentration was similarly calculated as the square root of the second moment of the actin intensity about the position of the window with the maximum integrated signal intensity. The square root of the second moment is essentially analogous to one standard deviation and was previously found empirically to a be a useful measure of growth cone length {Clarke, 2020 #6}. The global sqrt(2nd moment) was used for all subsequent quantitative analyses. For purposes of representation of positions on the axon (Fig 2E and 4E, F), it was found useful to indicate the partial sqrt(2nd moment) in the leading and trailing directions, but note that the global sqrt(2nd moment) does not, in general, equal the sum of the leading and trailing partial moments. Motion of the actin peak position was calculated between successive time points. For assessing correlation of actin peak motion during an interframe interval to static features of the axon, comparison was made to the static value at the start of that interval.

Statistical Methods

Repeated measures ANOVA was used to assess statistical significance of genotype comparisons. A linear model was generated, with first-order autoregression used as the covariance structure to account for repeated measures from each single cell. Box-Cox transformation was applied to outcome variables with non-normal distribution, using the Shapiro-Wilk test to assess normality of model residuals. Tukey's method was used to correct for multiple comparisons between the three genotypes. Where other statistical tests were applied they are specified in the text and figure legends (GraphPad Prism, Version 9).

Pairwise analysis of parameter correlations was quantified by the Kendall rank correlation (tau), with significance assessed by Benjamini-Hochberg FDR. Correlations were considered significant at FDR < 5% after correction for multiple testing

PCA was performed using standard methods of principal component regression. The PCA axes were defined by the eigenvectors of the correlation matrix of the seven parameters measured for each time point in the wild type dataset (specified in the text and listed in Fig 7). The first PC axis is along the eigenvector associated with the largest eigenvalue, the second PC axis is along the eigenvector with the second largest eigenvalue, etc. Data from the *UAS-FP4-mito* and *UAS-*

ena datasets were then visualized by projecting them into the PCA space determined from the wild type data. Determination of the PCA axes and projection of parameter data in the PCA space was coded in Python using the Numpy library routines.

Wavelet analysis

Wavelet analysis was performed using the Daubechies type 4 (D4) wavelet transform to quantify spatial frequency components of the actin distribution, with the transform modified to account for non-periodic boundaries. As described previously (Clarke *et al.*, 2020b), given N_B bins (equal to a power of 2) along the axon length, we define $S_{0,n}$ as the measured actin intensity in bin n. Let w be the bin width. We define the transform from spatial resolution $2^L w$ to spatial resolution $2^{L+1} w$ to be

$$S_{2,n} = \sum_{m=1}^{4} c_m \, S_{1,2n+m-2}$$

$$D_{2,n} = \sum_{m=1}^{4} d_m S_{1,2n+m-2}$$

Here L = 0 corresponds to the original binned intensities above, and for L, n takes values = 1, 2, ... N_B /2L. The coefficients { c 1, c 2, c 3, c 4 } = { $1 + \sqrt{3}$, $3 + \sqrt{3}$, $3 - \sqrt{3}$, $1 - \sqrt{3}$ }/4 x $\sqrt{2}$ specify an averaging filter, and { d1, d2, d3, d4 } = { c3, -c2, c1, -c0 } is a differentiating filter. The bin width w = 0.06 μ m, N_B = 2048, and the intensity of any bin outside of the axon is set to zero to avoid edge artifacts. See Supplemental Methods for a more conceptual explanation of wavelet analysis.

Jensen-Shannon Divergence (JSD)

Jensen-Shannon divergence was calculated for each cell between the starting actin distribution (p) and the distribution in each subsequent time point I using the formula:

$$JSD(p \| r) = \frac{1}{2} \sum_{n=1}^{n=N} \left[p_n \log_2 \left(\frac{2p_n}{p_n + r_n} \right) + r_n \log_2 \left(\frac{2r_n}{p_n + r_n} \right) \right]$$

where p and r are the two actin distributions and n is the normalized actin intensity of the nth bin of the distribution (n = 1,2, ... N). For three cells expressing *UAS-FP4-mito* (FP4-mito cell #1, #6 and #12) the absolute intensity of the LifeAct signal was quite low (nominal integrated actin intensity per time point < 5×10^4 arbitrary units), causing the resulting actin distributions to be discontinuous. Such distributions were not appropriate for JSD analysis and were excluded from this calculation.

Reproducibility and data exclusion

Movies were not collected or analyzed from cells that failed to show dynamics upon mounting, axons that grew out of the field of focus, or those for which image intensity was too low to detect. One cell (FP4-mito#7) had robust CD4-td-Tomato signal, but insufficient LifeAct-GFP intensity to segment in Imaris and MIPAV. Therefore, this cell was included in analysis of morphological features but not actin parameters. Sample randomization and blinding were not relevant to the experimental design. Sample size was selected based on leave-out analyses of datasets from previous experiments using this study design.

Data and code availability

Numerical data for all figures are included in Supplemental Datasheet S1. MIPAV code, including plug-ins, is freely available on the NIH website. Python scripts and all other primary data will be deposited in Mendeley upon publication.

Acknowledgements

We are grateful to all the members of our labs for their extensive contributions to the conception, execution, and interpretation of these experiments, particularly Ginger Hunter, Ram Kannan, and Arvind Shukla. We are also deeply grateful to Lenny Campanello for insightful critiques and suggestions concerning our analytical methods, Tianxia Wu for expert assistance with statistical analysis of our time course data, Camille Hanes for assisting in collection and analysis of endstage wing samples for determining terminal phenotypes of *ena*, and Joy Gu and Irina Kuzina for outstanding technical assistance throughout the course of these studies. We thank Holly Cline and David Miller III for their thoughtful comments on the manuscript. We are

also indebted to Julie Gates for providing the flies bearing *UAS-ena* and *UAS-FP4-mito-eGFP* transgenes without which these experiments could not have been performed. Spinning disc microscopy was performed in the Cytogenetics and Microscopy Core Facility of the National Human Genome Research Institute, with the invaluable assistance of Stephen Wincovitch. *Drosophila* stocks obtained from the Bloomington Drosophila Stock Center (NIH P4OOD018537) and antibodies from the Developmental Studies Hybridoma Bank were essential to these studies. This work was supported by an MURI grant to WG (AFOSR grant number FA9550-16-1-0052), National Science Foundation grants CHE-1800418 and CHE-2102684 to GAP, and by funds from the Basic Neuroscience Program of the Intramural Research Program of the National Institute of Neurological Disorders and Stroke of the National Institutes of Health (Z01-NS003013, to EG).

Competing interests

The authors declare no competing interests

Figure legends

Fig 1. Anatomy and measured parameters of TSM1

- A. Anatomy of TSM1. Z-projections of wing discs fixed and dissected at the indicated times. Neuronal membranes were labelled with anti-HRP (8hr APF image) or by expression of CD4-tdTomato (20hr APF image). Position of TSM1 cell body is indicated by white arrow; scale bar is at the bottom of each image.
- B. Time course of development of a typical wild type TSM1 axon, with membrane and actin, labelled, respectively, by expression of td-Tomato and LifeAct-eGFP. Z-projections are shown of image stacks collected at the indicated times by spinning disc confocal microscopy. Yellow arrow in the membrane images indicates a fixed position in the disc for comparison of axon length. Scale bar is indicated in the 18' image.
- C. List of parameters measured in all time points of all trajectories imaged. See Methods for details.
- D. For illustrative purposes, example of some of the quantified parameters from a single time point, taken from the axon whose membrane and LifeAct channels are shown

beneath. Blue line shows the distribution of integrated LifeAct fluorescence intensity along the axon, expressed in arbitrary units (a.u.); orange bars show the number of filopodial branches arising from the axon shaft in 5 μ m windows along the axon. Note that alignment with the image below is not exact as length is measured in 3-dimensional space, not in projection, and since some filopodia are not visible at this projection angle. Positions of the peaks of actin and of filopodial projections were identified using a 5 μ m sliding window, and are indicated with arrows. The "position" of the peak is defined as the midpoint of the window that has the highest integrated actin intensity or filopodial density, respectively. The "lengths" of the peak zones of actin and of filopodia were calculated as the square root of the 2nd moment of each distribution about its peak position, a measure corresponding essentially to \pm one standard deviation (brackets). See Methods and {Clarke, 2020 #6} for detailed explanation of the utility of this definition.

Fig 2. Dynamics of the growth of wild type axons.

A. Scatterplot of the positions of the peak of filopodial density ("filopodial peak") vs the actin peak for the entire wild type dataset. Note that many datapoints are concentrated along the line x = y (dashed black line); ie., positions of the actin and filopodial peaks correspond closely for many time points, however it is clear by inspection that the filopodial peak lags significantly behind the actin peak in a substantial number of time points – ie., off-line datapoints have a pronounced tendency to lie well below the line, rather than above it.

B. Tabulated offset between the positions of the peaks of actin and filopodia (in microns). Positive values are time points where the actin peak leads the filopodial peak. Median and interquartile range are shown; note that median > 0, and that the distribution is skewed heavily to larger positive than negative values.

C. Scatterplot of the motion of the filopodial peak (in microns) in the time interval $t \rightarrow t+1$ vs the offset between actin and filopodial peaks at time t. Spearman r = 0.34; p < 0.0001.

D. Scatterplot of the motion of the actin peak (in microns) in the time interval $t \rightarrow t+1$ vs the offset between actin and filopodial peaks at time t. Spearman r = -0.26; p < 0.0001.

E. Graph of the positions of the actin peak (blue), and of the trailing (purple) and leading (green) 'edges' of the actin peak, as a function of time, in a typical wild type trajectory. Trailing and leading edge positions were calculated as, respectively, the square root of the trailing and leading partial 2nd moments of the actin distribution. These are indicated as dashed lines to emphasize that they are statistical measures, not discrete axonal features. Positions are given in microns; time in minutes. Time axis increases downwards. Note the inconsistent nature of actin advance, with the peak position wiggling back and forth within the window that defines the actin mass at any given time.

F. Length of the actin peak (square root of the 2nd moment of the distribution) as a function of time in the same trajectory shown in E. Note the fluctuating nature of the length of the actin peak. The peak length graphed here, and used in all statistical analyses below, is based on the global second moment, whereas the positions graphed in panel 2E are calculated from the separate trailing and leading partial second moments. In general, the global 2nd moment does not equal the sum of the partial 2nd moments because of how these properties are calculated. The global moment is more appropriate for further statistical analyses, while the partial moments are more informative for aligning to visible features of the axon.

G. Scatterplot of the offset between the positions of the actin and filopodial peaks vs the length of the actin peak. Spearman r=0.25; p<0.0001.

Fig 3. Validation of transgenes for manipulating Ena activity

A, B. Anti-Ena immunolocalization of Ena protein in photoreceptor neurons of fixed third instar larva.

A. Control (*neur-GAL4*). Ena protein immunoreactivity (green) can be seen in small, widely distributed puncta (*cis*-Golgi compartment {Kannan, 2014 #62}) and along cell boundaries.

B. neur-GAL4; UAS-ena. Upon overexpression of Ena, Golgi compartment becomes concentrated in the basal portion of the photoreceptor cell body and recruits much of the endogenous Ena protein from the rest of the cell {Kannan, 2014 #62}. Coexpressed CD4-td-Tomato channel is shown (red) to facilitate visualization of neuronal membrane. Scale bar in panel B.

C,D. Anti-Fasciclin 2 immunostaining of fixed stage 17 embryos to visualize peripheral nerves. Scale bar in panel C.

C. Control (*neur-GAL4*). ISNb nerve is visible (brown DAB reactivity; arrow), associated with a layer of internal muscles. ISN is in a deeper focal plane (out of focus; dashed arrow).

D. neur-GAL4; UAS-FP4-mito-eGFP- expressing motoneurons display the ISNb axon misrouting typical of ena loss-of-function. ISNb projections are not observed in ventrolateral target zone (outlined with dashed oval), but rather, the axons remain associated with ISN in a deep plane of focus (arrow) and fail to arborize on muscles.

-E - I. Anti-Enabled antibody staining of fixed wing imaginal disc at 8h APF. E, F are single optical slices (scale bar in panel E);—G - I are z-projected image stacks (scale bars in panels G, H).

E. Control (neur-GAL4). Ena immunoreactivity in green.

F. neur-GAL4; UAS-ena. Signal from overexpressed Ena protein is clearly visible above the endogenous background of Ena immunoreactivity in sense organ cells along the wing margin, and specifically in the TSM1 cell body (arrow).

G. neur-GAL4, td-Tomato; UAS-ena, showing a projected Z-stack of TSM1 cell body, axon and growth cone. Green channel: anti-Ena; red channel: CD4-td-Tomato (membrane marker). In a fraction of filopodia, Enabled immunoreactivity becomes concentrated at the filopodial tip (yellow arrow), but more commonly, Ena signal is the same or weaker at the tip than in the rest of the filopodium (white arrows). Arrows are in the same position relative to the cell in both panels. Scale bar at lower left.

H. Control (*neur-GAL4*). Ena protein signal in magenta. TSM1 cell body is circled (identified by coexpression of CD4-td-Tomato; not shown).

I. In *neur-GAL4; UAS-FP4-mito-eGFP* expressing cells, endogenous Enabled protein colocalizes with mitochondria (green puncta, visualized with FP4-mito-eGFP). TSM1 cell body is circled. Compare anti-Enabled signal (magenta, I) with mitochondrial signal (green, I') and overlay (I")

J-L. Suppression of the Abl loss-of-function axonal phenotype upon co-expression of FP4-mito-eGFP. Anti-HRP immunostaining of fixed pupal wing (20h APF) to visualize the mature axonal projection of TSM1 and of the L1 and L3 peripheral nerves.

- J. Control (neur-GAL4). TSM1 and L3 nerve are indicated; scale bar is shown.
- K. neur-GAL4, UAS-Abl RNAi. Note stalled TSM1 growth cone (yellow arrow).

L. *neur-GAL4*, *UAS-Abl RNAi*, *UAS-FP4-mito-eGFP*. L1 nerve is restored (white arrow) and grows to fasciculate with L3 nerve. Note that *neur-GAL4*, *UAS-Abl RNAi* flies were bred to contain an additional UAS-transgene (*UAS-CD4-td-Tomato*, not shown) to ensure that affected and rescued genotypes carried equal numbers of UAS transgenes in their genome.

M. Quantification of L1 nerve defects in Abl RNAi with and without expression of FP4-mito-eGFP. Frequency of defects in L1 nerve at 20hr APF is indicated by bar graph. Black numbers above bar give the frequency of defects (including stalls, misrouting, splitting, or absence of the nerve). White numbers at the base of the bar are the number of wings examined. p-values of comparisons are indicated (χ -square test).

N-P. Typical terminal phenotypes of TSM1/L1 nerve upon gain- and loss-of-function of *ena* Anti-HRP immunostaining of 20h APF wings of the indicated genotypes

- N. Control (neur-GAL4). TSM1 is indicated with white arrow
- O. *neur-GAL4; UAS-FP4-mito*. Yellow arrow indicates stalled and branched TSM1 growth cone
- P. neur-GAL4; UAS-ena. Yellow arrow indicates stalled and misrouted TSM1 axon.

 Note that, in wild type, TSM1 fasciculates with its target zone on the L3 nerve by about 12 hours APF. The first few wing margin follower axons have begun to traverse this trajectory by

~19-20 hours APF, though followers seem generally to be delayed somewhat in *ena* gain- and loss-of-function.

Q. Quantification of TSM1 defects upon altering *ena* activity. Frequency of defects in L1 nerve at 20hr APF is indicated by bar graph. Black numbers above bar give the frequency of defects (including stalls, misrouting, or splitting of the nerve). White numbers at the base of the bar are the number of wings examined. p-values of comparisons are indicated (χ -square test). The frequency of TSM1 defects in UAS-FP4-mito is not significantly different from that in Abl RNAi; UAS-FP4-mito, above (p = 0.2; χ -square).

Fig 4. TSM1 axons with Ena loss- or gain-of-function grow similarly to wild type axons.

- A. Tabulated values of the motion of the actin peak between successive time points in all genotypes. Distances in microns; 3' time steps for all trajectories. Median and interquartile ranges are shown.
- B. Tabulated values of the offset between the positions of the actin and filopodial peaks in all time points of *ena* loss of function (*UAS-FP4-mito*) and gain of function (*UAS-ena*). Median and interquartile range are shown. Median offset is significantly positive for *UAS-FP4-mito* (p<0.0001; Wilcoxon signed rank); for *UAS-ena* the median is not different from 0 by a statistically significant amount (p > 0.05), but interquartile range shows that the distribution trends toward positive values (actin peak leading branching peak). Compare with Fig 2B for the offset values in wild type.
- C. Morphology of a typical TSM1 growth cone in *neur-GAL4; UAS-FP4-mito-eGFP*. CD4-td-Tomato signal is shown, with scale bar.
- D. Morphology of a typical TSM1 growth cone in *neur-GAL4; UAS-ena*. CD4-td-Tomato signal is shown, with scale bar.

E, F., Graph of the positions of the actin peak (blue), and of the trailing (purple) and leading (green) 'edges' of the actin peak, as a function of time, in typical trajectories of actin loss-and gain-of-function, as described in Fig 2E.

G, H. Length of the actin peak as a function of time in the same trajectories shown in C, D. Compare with wild type (Fig 2F).

Fig 5. Comparison of single growth cone parameters in wild type vs altered-Ena conditions.

Values of indicated growth cone parameters were tabulated for all three genotypes. Statistical significance of differences is as indicated. Error bars indicate mean and SD. Statistical significance is indicated as follows for this and subsequent figures: *p < 0.05; **p < 0.01; ***p < 0.001; ****p < 0.0001. Comparisons that are not marked were not formally significant. See Methods for details of how significance was assessed.

- A. Total filopodial number
- B. Total filopodial length
- C. Average filopodial length
- D. Average filopodial order
- E. Length of actin peak (square root of the global 2nd moment of the actin distribution).
- F. Plot of the ratio of the average coefficient for each spatial order of the wavelet transform for *UAS-FP4-mito/UAS-ena*. Wavelet analysis quantifies the spatial structure of the actin distribution, with higher-order wavelets reflecting the frequency of local actin concentrations at short length scales, and lower-order wavelets reflecting spreading of actin density at longer length scales (see text and methods, and also {Clarke, 2020 #7} for additional explanation). The maximum at wavelet order 5 indicates that expression of *FP4-mito* causes the actin distribution to be spread out significantly on a length scale peaking at 6.5-25.6 μm, relative to that in *UAS-ena*, consistent with broadening of the actin peak by reduction of Ena activity. Asterisks indicate the significance of the difference in coefficient values for the indicated order between these two genotypes. For comparison of each altered-Ena genotype to wild type, and table listing the spatial range corresponding to each wavelet order, see Suppl Fig 2.

- G I. For each trajectory of each genotype, Jensen-Shannon Divergence (JSD) of the shape of the actin distribution was calculated between the first time point vs each subsequent time point. Divergence can vary from 0 (identical distributions) to 1 (unrelated distributions). For clarity, plots are shown here for only three illustrative trajectories of each genotype. For plots of JSD vs time for all trajectories, see Suppl Fig 3.
- J. Tabulation of the correlation of JSD vs time for all trajectories of each genotype (Kendall tau correlation value). Black bar indicates median value; asterisks indicate significance of genotype differences as specified above.

Fig 6. Pairwise correlations of parameters among time points of each ena genotype

- A. Table of pairwise correlation of the seven parameters reported for each time point (Kendall tau correlation). Correlation significance was calculated by the Benjamini-Hochberg method. Tau value is shown for all correlations with a false discovery rate (FDR) < 5%. Tau values in blue wild type; red *UAS-FP4-mito* (Ena loss-of-function); green *UAS-ena* (Ena gain-of-function). For table of all tau values and associated p-values, see Suppl Figs 4A and B, respectively.
- B. Filopodial number, length and order were significantly correlated in all pairwise combinations in all three genotypes. Tau values are shown.
- C. Scatterplot of motion of the peak of branch density in a given time step vs offset between the actin and filopodial peaks at the beginning of that time step for *UAS-FP4-mito*. Compare to wild type (Fig 2C). Spearman r = 0.24; p < 0.0001.
- D. Scatterplot of motion of the peak of filopodial density in a given time step vs offset between the actin and filopodial peaks at the beginning of that time step for *UAS-ena*. Compare to wild type (Fig 2C). Spearman r = 0.41; p < 0.0001.

Fig 7. Principle component analysis of all parameters for each *ena* genotype.

A, B. Fractional contribution to each of the first two principle components is shown for each measured parameter. (Contribution)² is shown to facilitate comparison.

- C F. PCA was performed on wild type using all 7 parameters, and data from *UAS-FP4-mito*, and *UAS-ena* datasets were then projected into the wild type PCA space. The plane corresponding to PC 1 and 2 is shown. C E show the three genotypes individually; D shows the overlay of all 3 genotypes.
- G. PCA of wild type is shown with each imaged cell colored separately. Note separation of trajectories into a cluster of three cells with PC1 less than approximately -0.5, and a second cluster with PC1 greater than that value.
- H J. Histogram of PC1 values for the three *ena* genotypes, as indicated. Note the bimodal distribution of PC1 in wild type; coincidence of PC1 values of FP4-mito with the higher-value wild type cluster, and PC1 values of *UAS-ena* concentrated roughly around the value of the minimum in PC1 values of wild type.

Legends to Supplemental Figures

Supplemental Figure 1. Schematic of imaging mount

Wing discs were mounted in a drop of Schneider's medium with 10% serum on a #1.5 coverslip and sealed with halocarbon oil to the underside of an air-permeable 35mm Lumox dish. The dish was filled with medium (to minimize reflection) and imaged by spinning disc confocal microscopy on an inverted microscope. See Methods for further details of the mounting method.

New Suppl Figure 2. Annotated control images for *ena* reagents

A., B. Anti-Ena immunolocalization of Ena protein in photoreceptor neurons of fixed third instar larvae. These are the same images shown in Figure 3A, B but with boundaries of two cells outlined in white to assist identification (insets). (A) control. Green: anti-Ena (B) *neur-GAL4*, *UAS-CD4-td-Tomato*; *UAS-ena*^{WT}. Green: anti-Ena; Red: CD4-td-Tomato.

C. Anti-Ena immunostaining of control wing disc fixed 7.5h APF. TSM1 membrane is visualized by expression of CD4-td-Tomato (red); anti-Ena signal is in green. Arrows indicate equivalent locations in the separated channels. TSM1 cell body (marked by asterisk) can be detected,

faintly, in the anti-Ena image (right panel). Hints of fragments of the axon can perhaps be discerned vaguely in places, but they are neither continuous nor reliably distinguishable above the background of epithelial labeling.

D. Anti-Ena immunostaining of wing disc of *neur-GAL4*, *UAS-CD4-td-Tomato*; *UAS-FP4-mito-eGFP* fixed 7.5h APF. CD4-td-Tomato in red; both anti-Ena and UAS-FP4-mito-eGFP are in green. Top panel shows the complete TSM1 with green channel intensity reduced to avoid saturating the punctate signal in the cell body. Area indicated by white outline is shown below with green channel enhanced to attempt to detect either Ena immunoreactivity or localization of FP4-mito-eGFP in the TSM1 axon. Neither is seen reliably; occasional puncta that overlap the td-Tomato axonal signal cannot be distinguished from Ena immunoreactivity in the associated epithelium. White arrows indicate equivalent locations in the separated channels. Use of a different fluorochrome (Alexa-647) for detection of anti-Ena did not provide detectable axonal signal in a parallel experiment. In the top panel, FP4-mito-eGFP signal is detected outside the boundaries of the TSM1 neuron itself due to expression of the transgene in associated sense organ support cells.

Supplemental Figure 3. Wavelet coefficients for all genotypes

- A. Average (amplitude)² was calculated for each wavelet order from all datapoints for each genotype. Plotted here are the ratio of the (amplitudes)² for *UAS-FP4-mito*/wild type (blue) and *UAS-ena*/wild type (orange).
- B. Table listing the spatial range corresponding to each wavelet order in this dataset

Supplemental Figure 4. Jensen-Shannon divergence of actin distribution of initial time point vs subsequent time points for all trajectories.

Plot of the Jensen-Shannon divergence, calculated between the actin distribution of the starting point of each trajectory and every subsequent time point of that trajectory, vs time. Divergence can vary between 0 (identical distributions) and 1 (unrelated distributions). Time points are numbered on the x-axis, and legend shows the color code identifying the imaged cell. Note that

low absolute intensity of the LifeAct signal in three cells expressing FP4-mito caused the measured actin distribution to be discontinuous, and therefore inappropriate for calculation of JSD. Those cells were excluded from this analysis.

Supplemental Figure 5. Pairwise correlations of all measured parameters for all genotypes

Kendall tau correlation was calculated for all pairwise combinations of the indicated parameters

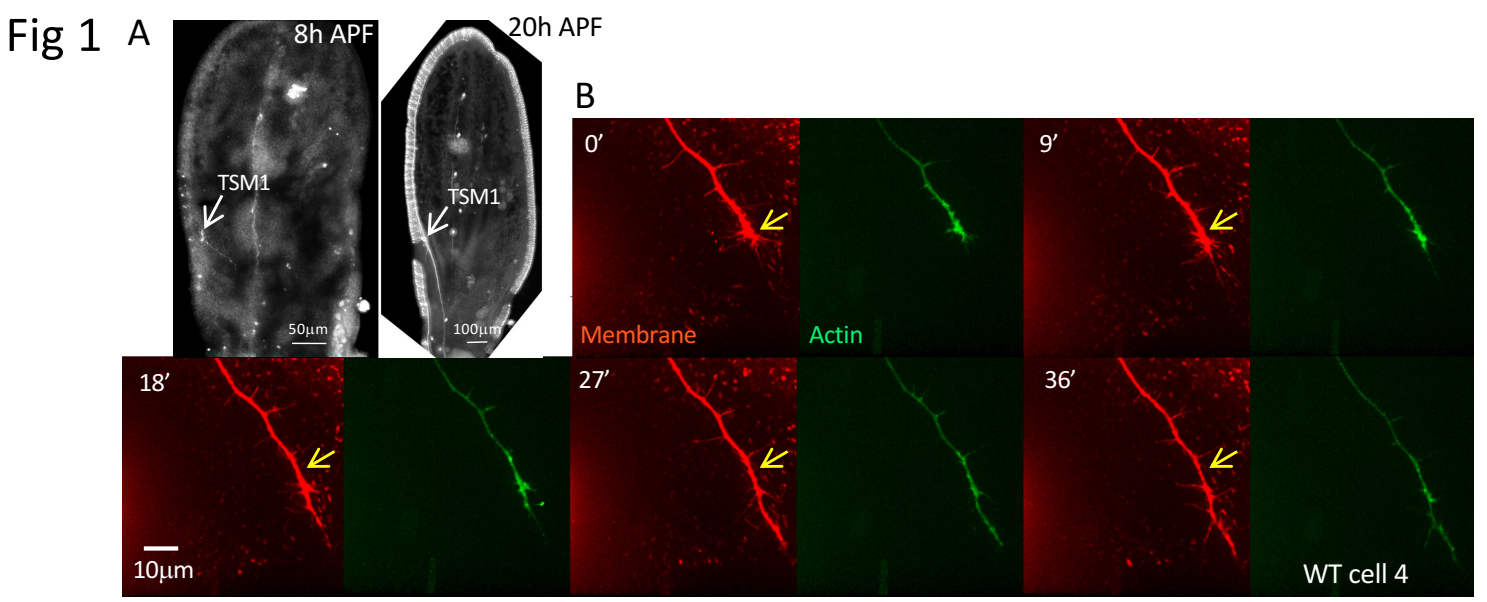
for every timepoint of each cell imaged, and significance assessed by the Benjamini-Hochberg

method. Data for wild type is shown in blue, *UAS-FP4-mito* in red, and *UAS-ena* in green.

- A) Correlation value: Kendall tau
- B) Statistical significance: p-value; critical value for FDR < 5% for each genotype (corrected for multiple testing) is indicated at the bottom.

Supplemental Figure 6. PCA of growth cone parameters, coded by cell and by genotype

- A. PCA is shown for *UAS-Ena* and *UAS-FP4-mito* time points, coded by trajectory. Note that UAS-Ena trajectories fail to split into distinct classes PC1 < and > -0.5.
- B. PC2 values were tabulated for all datapoints of each genotype. Mean and SD are indicated.



C Parameters measured:

- 1. Total filopodial number
- 2. Total filopodial length
- 3. Average order of filopodial projections
- 4. Length of protrusive filopodial peak
- 5. Length of actin peak

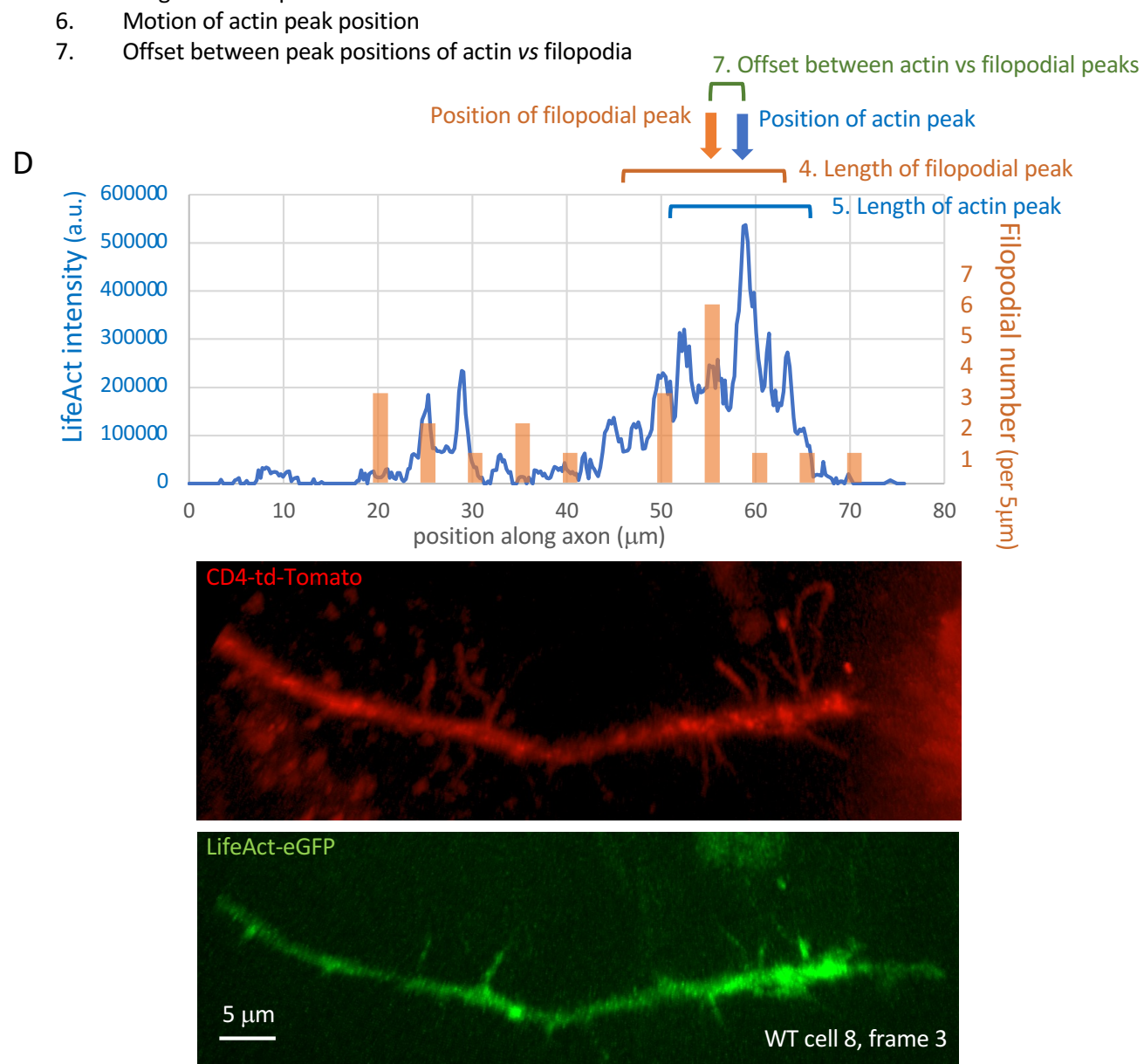


Fig 2 Α В Position of filopodial peak Offset between peaks of actin vs filopodia (μm) -50 WT Position of actin peak C D Motion of filopodial peak (µm) Motion of actin peak (μm) r = 0.34 p < 10⁻⁴ -25 -20 r = -0.26-40 p < 10⁻⁴ -60 -80 -80 Offset between peaks of actin vs filopodia (µm) Offset between peaks of actin vs filopodia (µm) Position along axon (µm) Ε WT (cell 4) Time (min) actin peak -- back of actin peak -- front of actin peak F Offset between peaks of $\, \Omega \,$ Length of actin peak WT actin vs filopodia (µm) 15 r = 0.25p < 10⁻⁴ WT (cell 4) -20 Time (min) -40 Length of actin peak (µm)

Fig 3

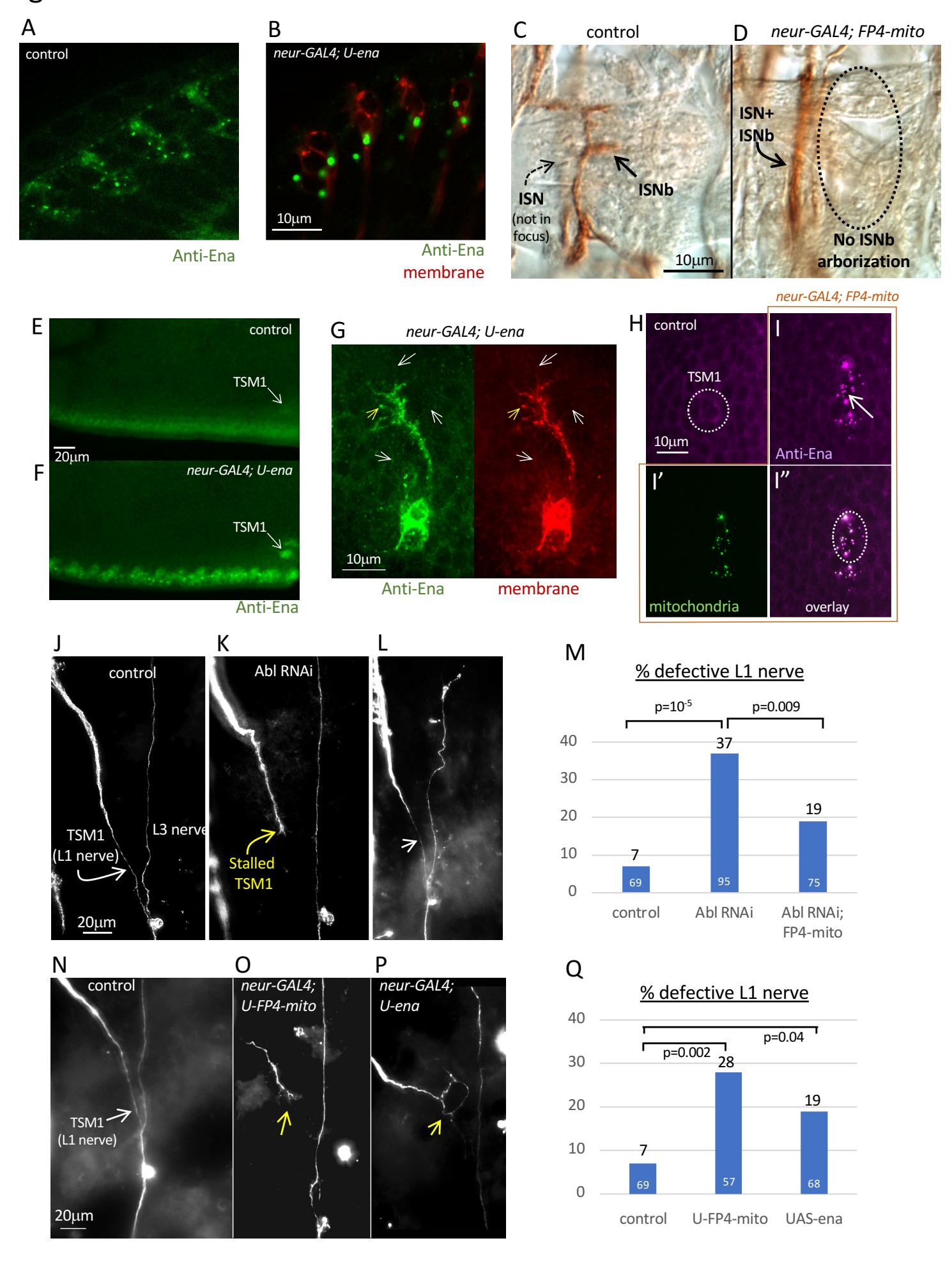
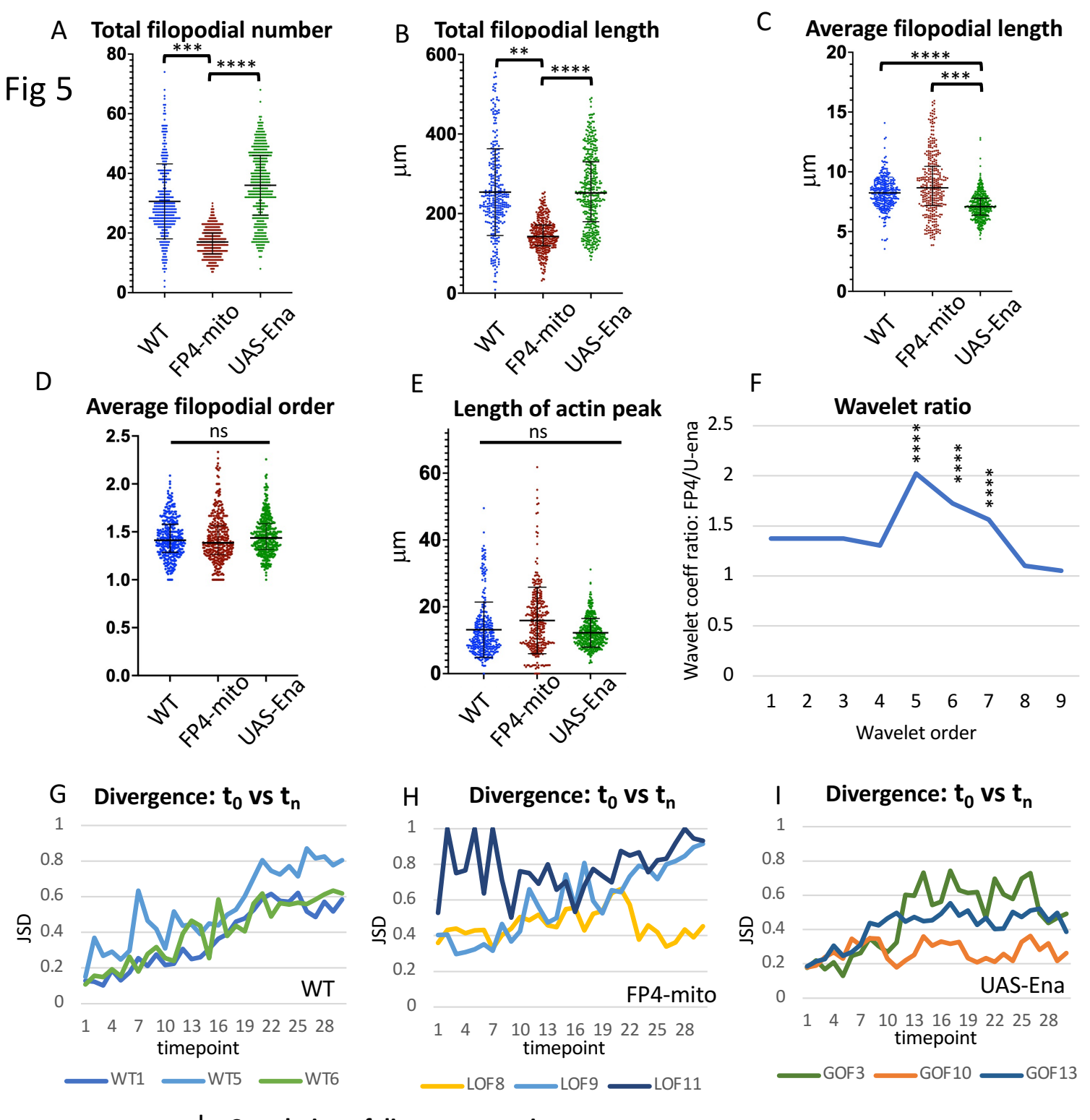
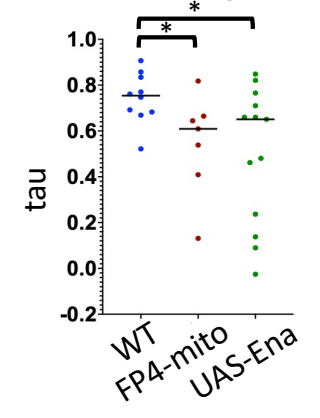
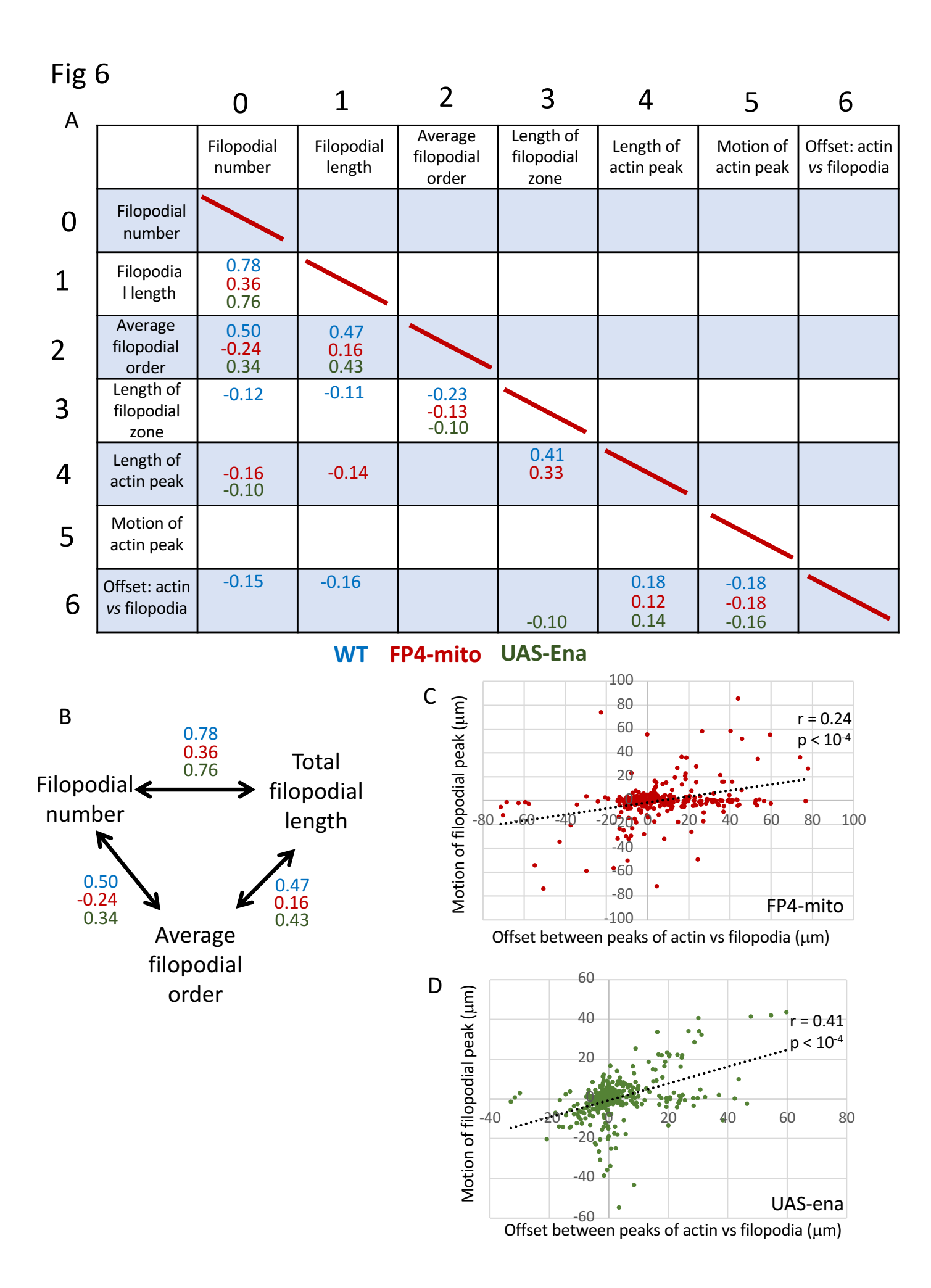


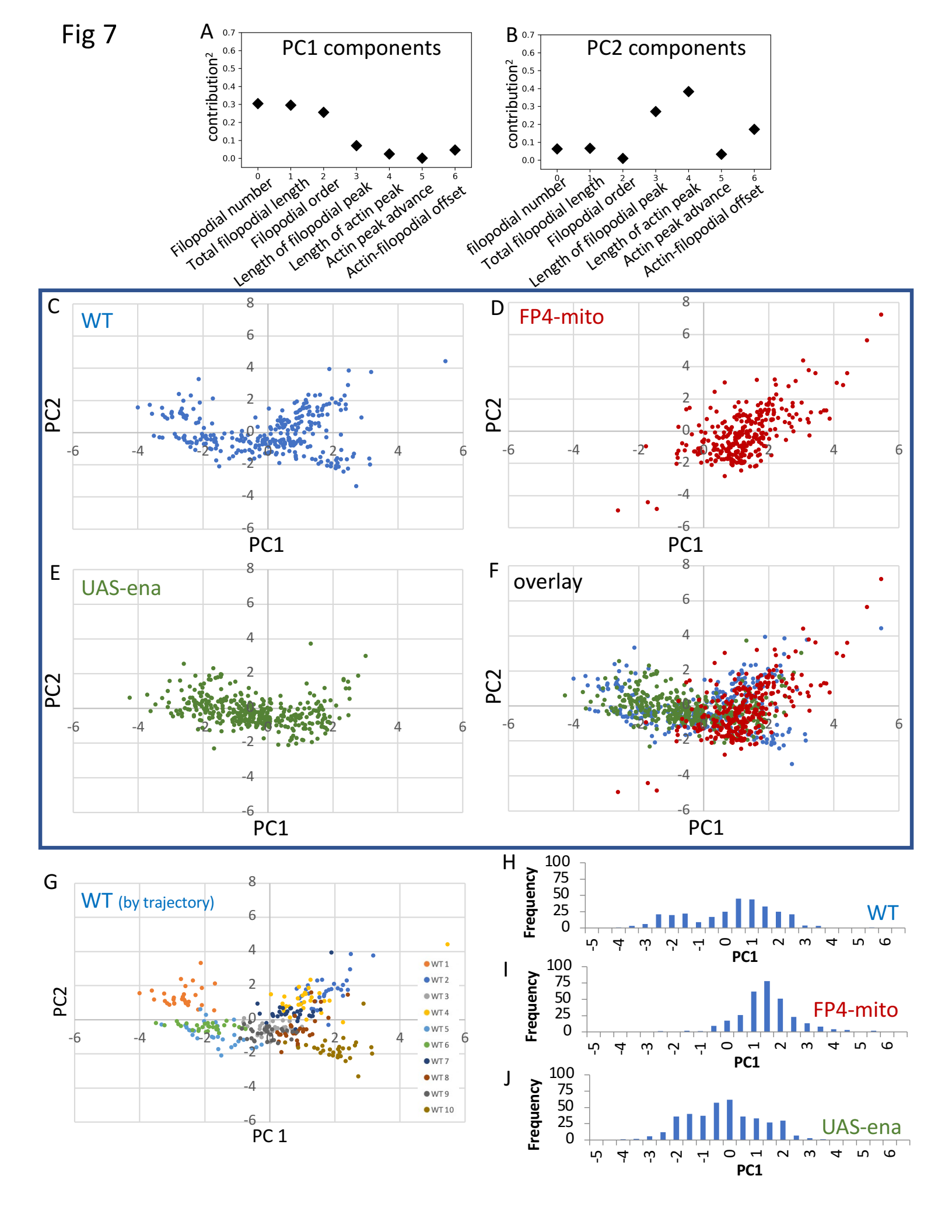
Fig 4 В 100-1003 ns Motion of actin peak position per 3' time step (µm) Offset between peaks of actin vs filopodia (μm) **50 50** 0 0 -50 -50 -100 -100 FPA-mitO JAS-Ena WI LPA-mito UAS-Ena D C 10μm 10μm FP4-mito cell 11, frame 18 U-ena cell 6, frame 21 F Ε Position along axon (µm) Position along axon (µm) 45 50 55 60 70 80 100 35 40 65 70 60 0 0 UAS-Ena FP4-mito 10 10 (cell 4) (cell 7) Time (min) 20 20 Time (min) 30 30 40 40 50 50 60 60 70 80 80 90 90 peak position ---- rear of peak position of peak ---- rear of peak -- front of peak -- front of peak G 16 Length of actin peak (µm) FP4-mito Н 14 (cell 4) **UAS-Ena** 12 12 Length of actin peak (cell 7) 10 10 8 8 (mm) 6 6 4 40 50 60 0 10 20 30 70 80 90 0 40 50 10 20 30 60 70 80 90 Time (min) Time (min)



Correlation of divergence vs time

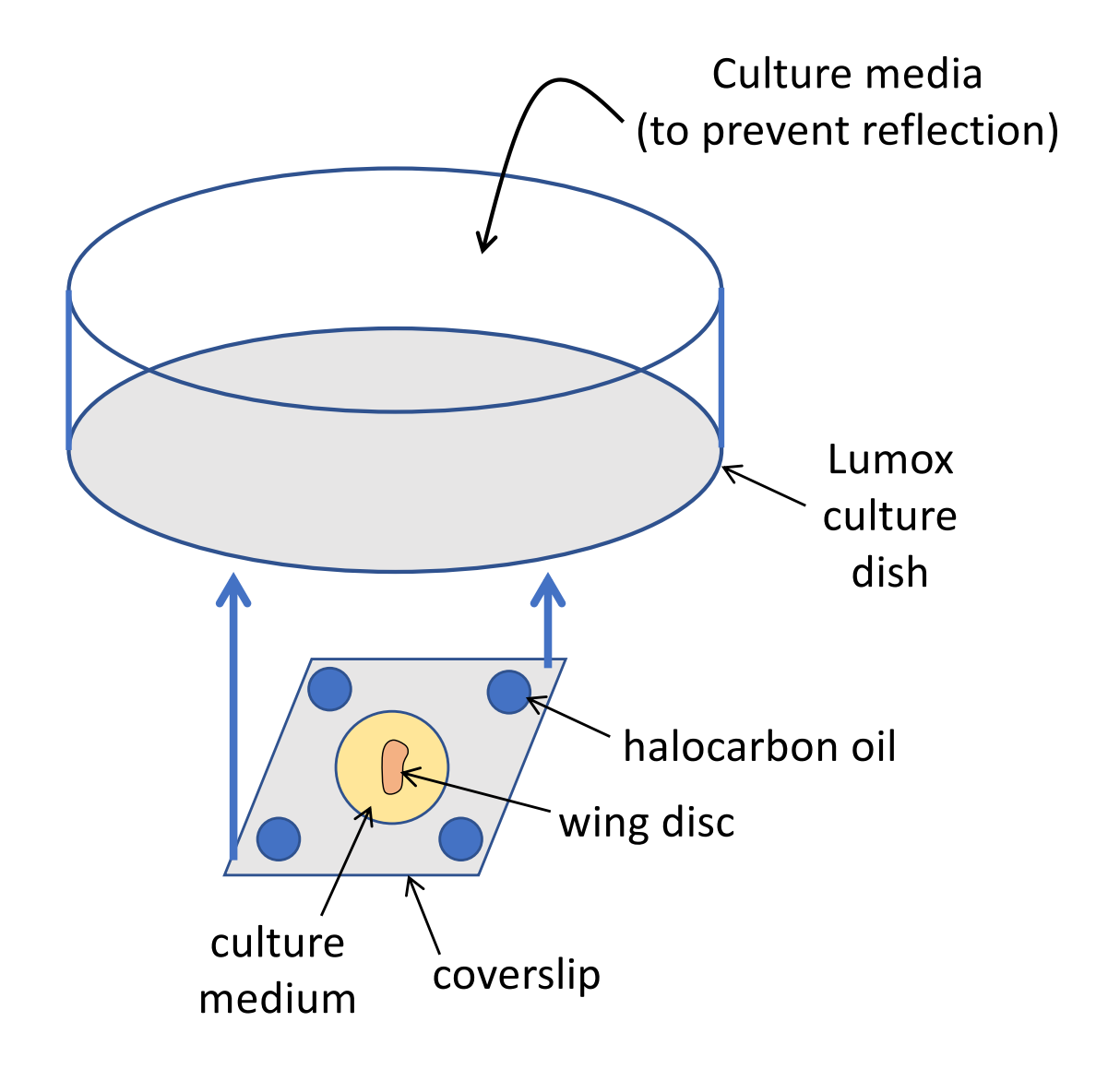






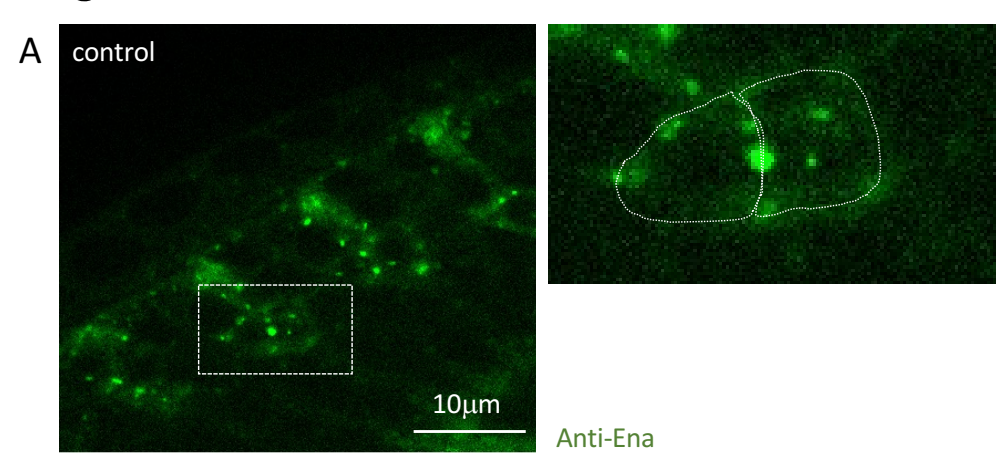
Suppl Fig 1

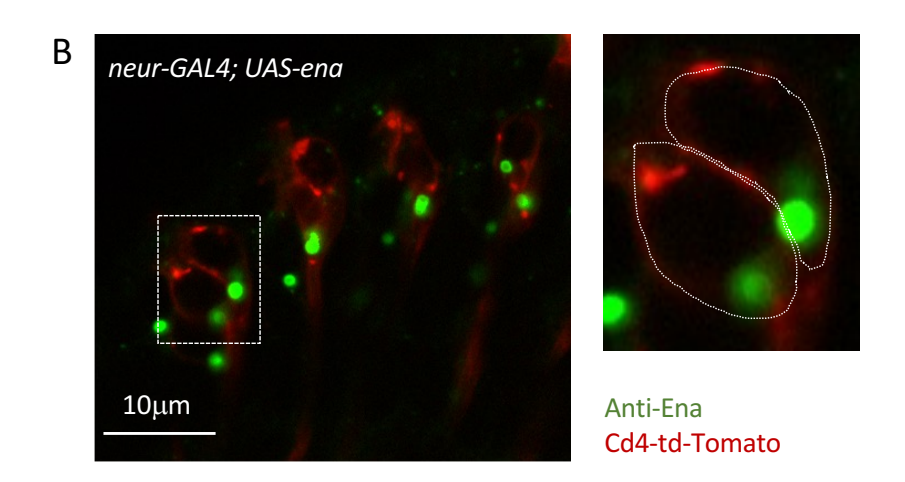
Schematic of imaging setup

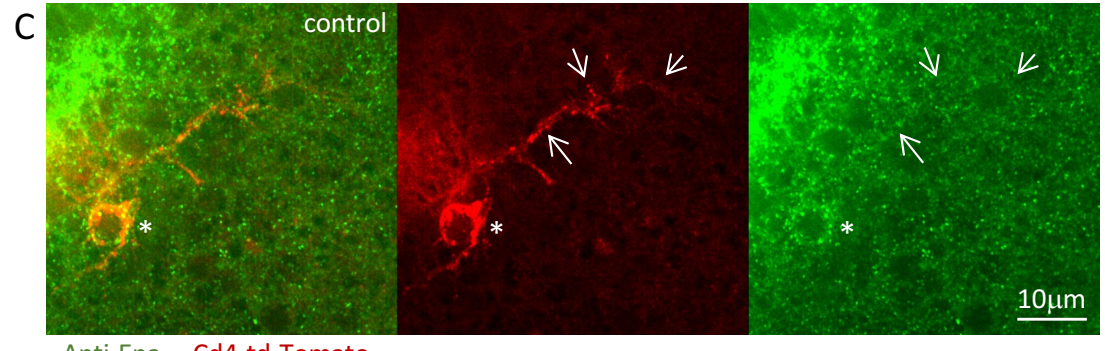


(Image from beneath)

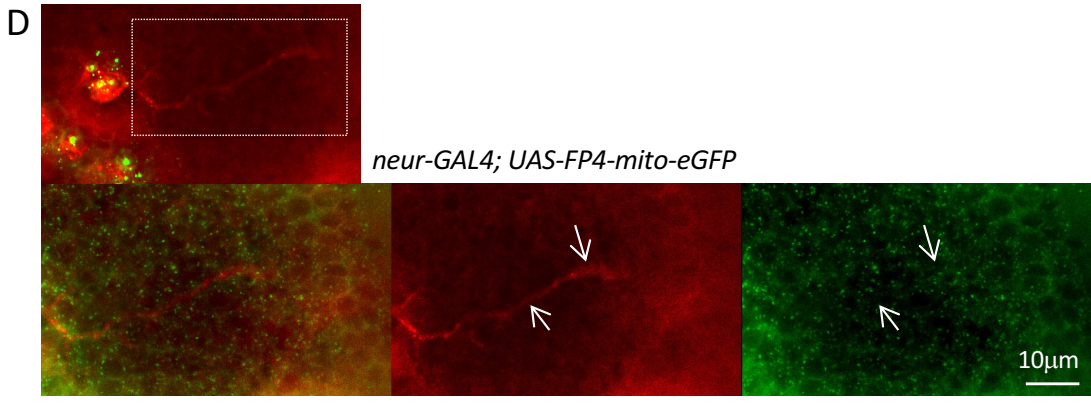
Suppl Fig 2











(Anti-Ena + FP4-mito-eGFP) Cd4-td-Tomato

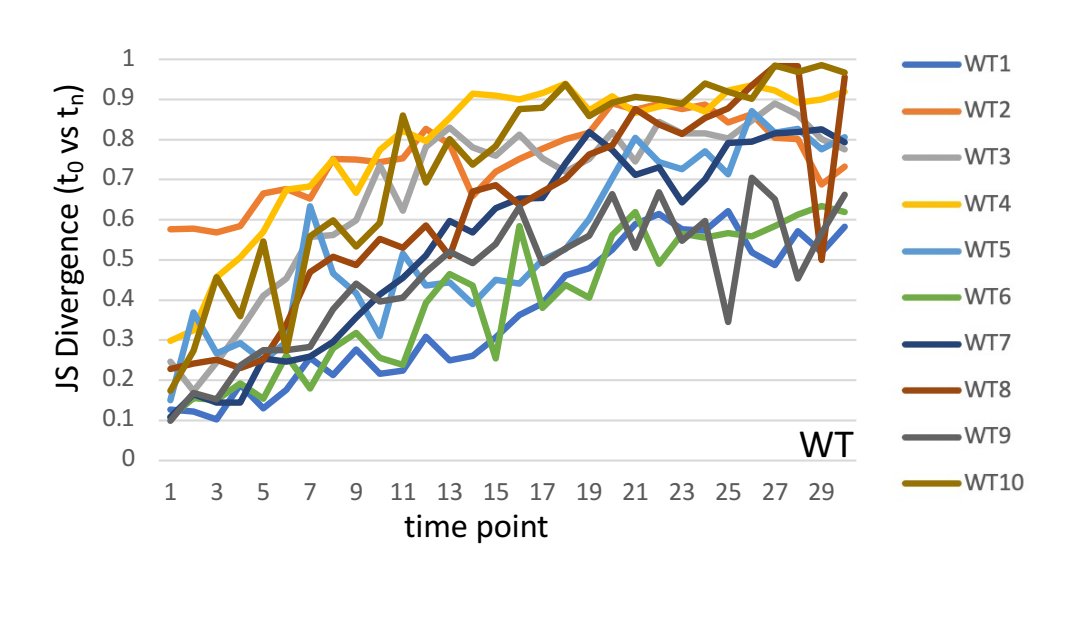
Suppl Fig 3

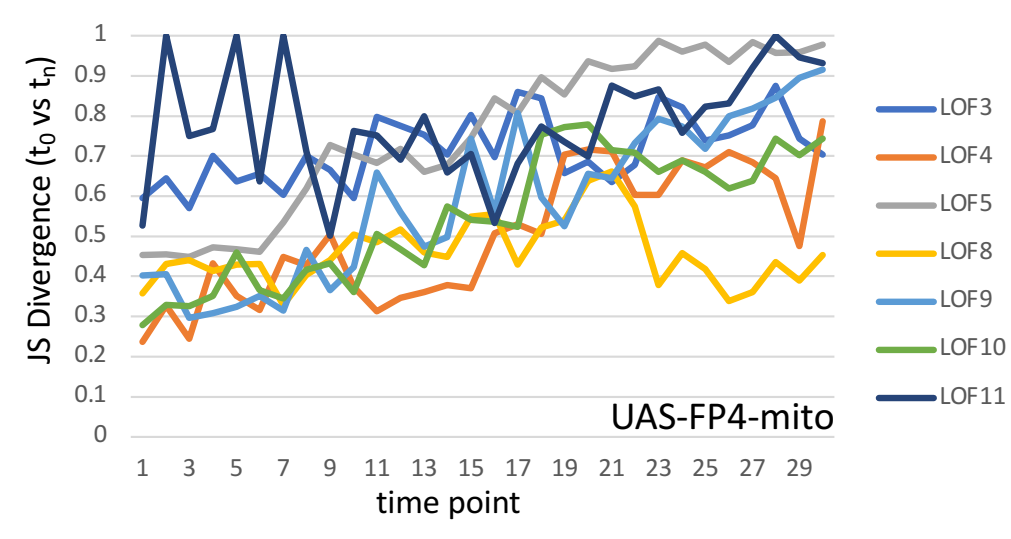


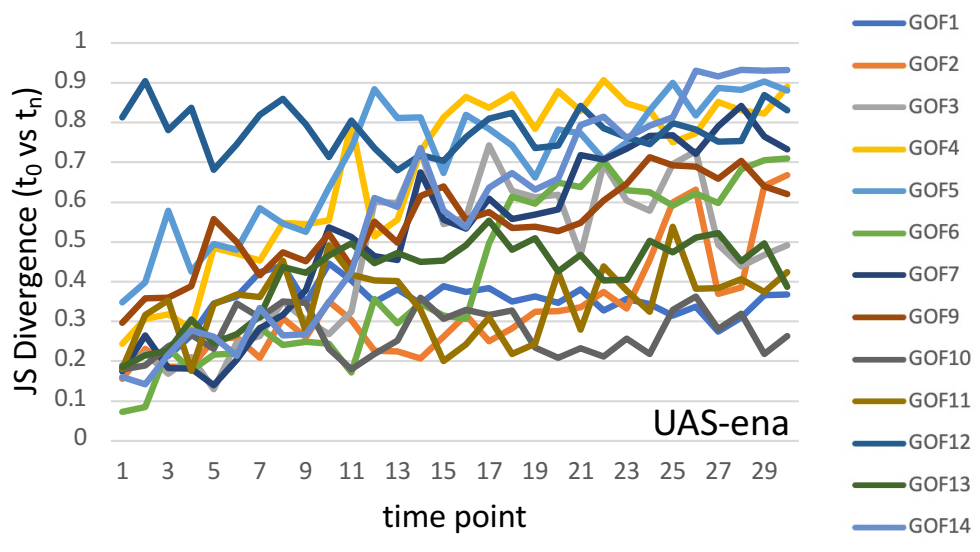
В

Wavelet order	Contributing spatial range					
1	> 102.4 μm					
2	> 51.2 μm					
3	25.6 - 102.4 μm					
4	12.8 - 51.2 μm					
5	6.4 - 25.6 μm					
6	3.2 – 12.8 μm					
7	1.6 - 6.4 μm					
8	0.8 - 3.2 μm					
9	0.4 - 1.6 μm					

Suppl Fig 4







Α

В

Correlation (Kendal tau)

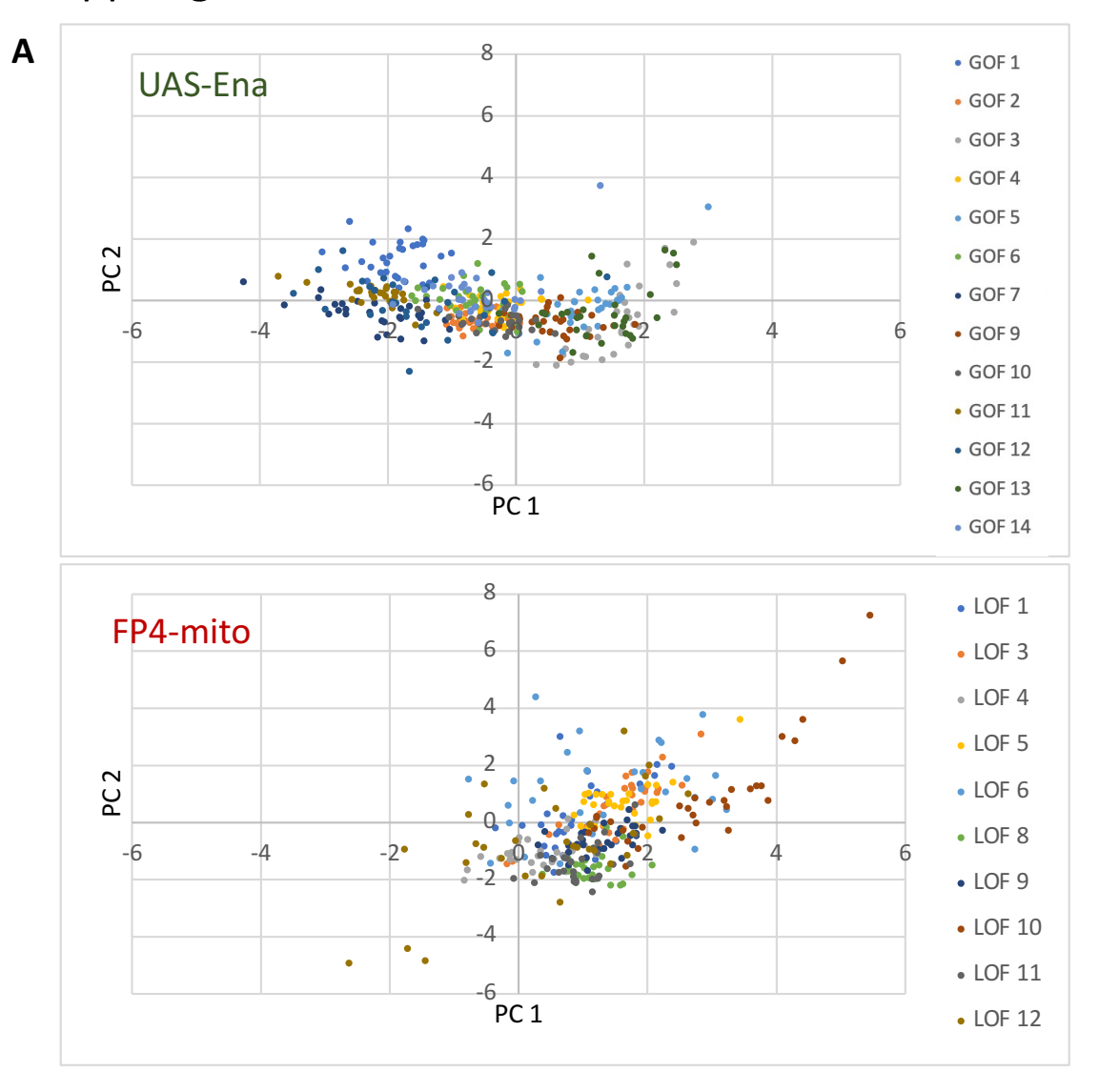
	Correlation (Kendar tad)									
	Filopodial number	Filopodial length	Average filopodial order	Length of filopodial zone	Length of actin peak	Motion of actin peak	Offset: actin vs filopodia			
Filopodial number						<u>Legend:</u> WT UAS-FP4-mito UAS-Ena				
Filopodial length	0.78 0.36 0.76	/								
Average filopodial order	0.50 -0.24 0.34	0.47 0.16 0.43	/							
Length of filopodial zone	-0.12 -0.05 -0.01	-0.11 0.04 -0.05	-0.23 -0.13 -0.10							
Length of actin peak	0.04 -0.16 -0.10	0.02 -0.14 -0.09	-0.03 -0.10 0.01	0.41 0.33 0.07						
Motion of actin peak	0.003 -0.02 -0.01	-0.01 0.04 -0.01	0 0.01 -0.003	-0.004 0.03 -0.03	-0.03 -0.03 -0.09					
Offset: actin vs filopodia	-0.15 -0.10 -0.05	-0.16 0.05 -0.06	-0.09 0.05 -0.09	0.05 0.05 -0.10	0.18 0.12 0.14	-0.18 -0.18 -0.16				

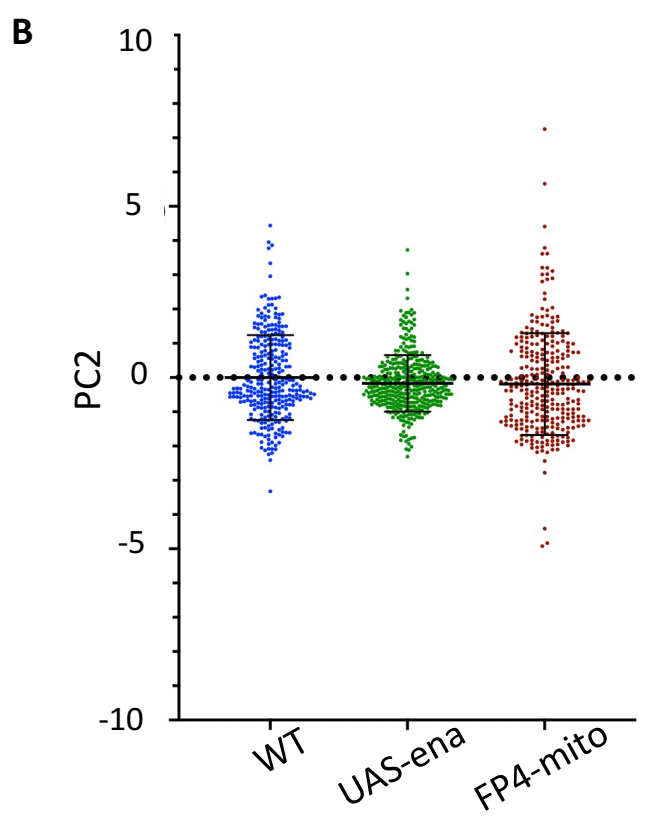
p-value

p value								
	Filopodial number	Filopodial length	Average filopodial order	Length of filopodial zone	Length of actin peak	Motion of actin peak	Offset: actin vs filopodia	
Filopodial number	/					Legend: WT UAS-FP4-mito UAS-Ena		
Filopodial length	5.5E-88 6.8E-20 9.5E-109							
Average filopodial order	3.7E-37 2.9E-9 1.8E-23	1.3E-33 6.3E-5 2.2E-36	/					
Length of filopodial zone	0.001 0.17 0.88	0.006 0.36 0.11	1.7E-9 7.5E-4 0.003					
Length of actin peak	0.33 5.8E-5 0.004	0.63 3.5E-4 0.01	0.42 0.01 0.72	8.7E-26 1.0E-17 0.05	/			
Motion of actin peak	0.94 0.68 0.81	0.89 0.28 0.77	0.99 0.80 0.93	0.93 0.50 0.41	0.50 0.50 0.01			
Offset: actin vs filopodia	1.2E-4 0.01 0.11	5.9E-5 0.19 0.07	0.02 0.16 0.01	0.21 0.24 0.01	5.3E-6 0.001 3.5E-5	3.8E-6 1.8E-6 3.41E-6		

Critical value for BH FDR < 5%: WT: 0.0063 FP4-mito: 0.0019 UAS-Ena: 0.004

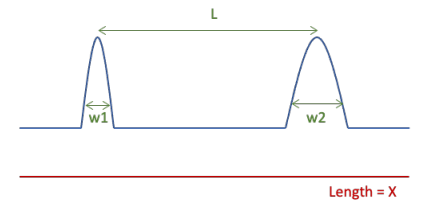
Suppl Fig 6



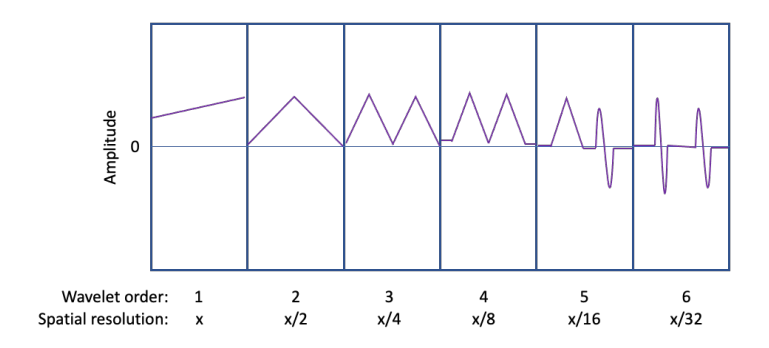


Disclaimer: We will attempt here to explain the essence of the wavelet method in non-mathematical terminology. That is a fraught enterprise, and we apologize in advance for the inevitable oversimplifications and inaccuracies. For an excellent conceptual introduction to wavelets we suggest https://towardsdatascience.com/the-wavelet-transform-e9cfa85d7b34

Imagine a simple, 1-dimensional distribution, like the one below, with a total length X. It has two peaks, one that has a width of w1 and another with a width of w2, which are separated from each other by a distance L.



Now let us consider wavelet analysis of this distribution. The point of this process will be to query the distribution at a series of spatial resolutions, from the highest resolution (querying short spatial distances) down to low resolution (where the entire distribution looks like a single element). The goal is to ask, for each size range, whether there are features in the original distribution, or spacings of features, that are in the size range defined by that wavelet order. We start by selecting a simple waveform that is used as a mathematical filter to query the distribution. Different waveforms can be used for this purpose depending on the nature of the distribution we want to analyze; here we have used a common form called a Daubechies 4 wavelet. The period of the filtering waveform is much smaller than the length X of the target distribution and it acts, in essence, as a kind of edge-detector. The wavelet is applied locally (by matrix multiplication) to the values of a groups of points at one end of the distribution, then stepped laterally to an overlapping group of points, then to the next, and to the next, etc., in the manner of a sliding window. At each point it will be multiplied by the values of the distribution to be analyzed. When the process is finished, it produces a filtered form of the original distribution that has half the resolution of the starting distribution. That filtered form is then subjected to the same procedure to produce the next lower order, and then repeated again, each time reducing the resolution by a factor of 2, until we reach the point that the entire distribution acts as a single entity.



To think about what this does, it is easiest to start from the lowest resolution data and work our way to high resolution. In the example shown here, the 1st and 2nd orders simply show there is a signal somewhere in the distribution. The resolution is too low to tell more. In the 3rd order, the resolution is sufficient to show that two peaks are present but not to give detailed information about either one (ie., the resolution is better than length L, but is not high enough to dissect the properties of elements as small as w1 or w2). Once we get to 5th order, the resolution of the process is sufficient to distinguish the leading from the trailing edge of the broader peak (w2), so we see a more complex waveform for w2; ie., we can infer the approximate width of the peak. It is not, however, sufficient to detect the fine structure of w1. At 6th order, the analysis now has sufficient resolution to infer the widths of both peaks, w1 as well as w2. If there had been even finer detail to the structure of w1 (or w2), then it would have been necessary to take the analysis to yet higher orders to resolve that.

So the wavelet analysis allows us to measure the distribution of information in a starting curve: is the signal homogeneous or clumpy, and to the degree that it is clumpy, how wide are those clumps and how are they distributed along the length of the curve. In our actin analysis we are not using it to measure individual features of a single curve, but instead we average over all the timepoints for each trajectory, and over all the cells of a given genotype. Comparing the amplitudes obtained by that averaging across orders and across genotypes allows us to quantify how much each spatial scale is contributing to the global distribution of actin under different conditions.

In this paper, we use the wavelet method (rather than Fourier analysis, for example, which can also quantify spatial contributions to a distribution) because it is extremely effective for non-periodic curves with non-repeating, local features. This is particularly true if there are sharp discontinuities in the signal, as we have in an actin distribution in an axon. But in the context of the current paper, the key point is that it provides a rigorous way to define and quantify the way actin is distributed, globally, along an axon and to compare the distributions that form in different genotypes.